Available online at www.sciencedirect.com

ScienceDirect

Journal of Magnesium and Alloys 10 (2022) 2919–2945

www.elsevier.com/locate/jma

Review

Grain refinement of Mg-alloys by native MgO particles: An overview

Z. Fan*, F. Gao, Y. Wang, S.H. Wang, J.B. Patel

Brunel Centre for Advanced Solidification Technology (BCAST), Brunel University London, Uxbridge, UB8 3PH, UK

Received 25 July 2022; received in revised form 27 September 2022; accepted 10 October 2022
Available online 12 November 2022

Abstract

A fine and equiaxed solidification process delivers multidimensional benefits to Mg-alloys, such as improved castability, reduced casting defects, enhanced mechanical properties, increased corrosion resistance and potential for increased recycled contents. Despite extensive research on grain refinement of Mg-alloys in the last few decades, currently, there is no effective grain refiner available for refining Mg-Al alloys, and our current understanding of grain refining mechanisms is not adequate to facilitate the development of effective grain refiners. Under the EPSRC (UK) LiME Hub's research program, substantial advances have been made in understanding the early stages of solidification covering prenucleation, heterogeneous nucleation, grain initiation and grain refinement. In this paper, we provide a comprehensive overview of grain refinement of Mg-alloys by native MgO particles. We show that native MgO particles can be made available for effective grain refinement of Mg-alloys by intensive melt shearing regardless of the alloy compositions. More importantly, we demonstrate that (1) the addition of more potent exogenous particles will not be more effective than native MgO; and (2) MgO particles are difficult to be made more impotent for grain refinement through promoting explosive grain initiation. We suggest that the most effective approach to grain refinement of Mg-alloys is to make more native MgO particles available for grain refinement through dispersion, such as by intensive melt shearing.

Keywords: Mg-alloys; Grain refinement; Magnesia (MgO); Nucleation; Grain initiation.

1. Introduction

Magnesium (Mg) alloys offer unique engineering properties, such as low density, high specific strength, excellent castability and good recyclability. Therefore, they find extensive applications in a wide range of industrial sectors, such as automotive, aerospace and portable electronic devices and bio-medical industries [1–5]. Particularly, applications of magnesium in the automotive industry are continuing to increase as automobile manufacturers are seeking to decrease vehicle weight for the reduction of CO_2 emissions [5].

Compared with Al-alloys, another member of the light-alloy family, Mg-alloys have some limitations, such as low creep resistance, low tensile properties, poor workability and low corrosion resistance. Hence, tremendous efforts have been made to overcome such limitations through various approaches, such as the addition of alloying elements [6–9], surface coating [10,11] and grain refinement [12–15]. Among these approaches, grain refinement of Mg-alloys provides multi-dimensional benefits: (1) a fine and equiaxed solidification process facilitates the casting process and thus reduces cast defects in the solidified microstructures [3]; (2) the unusually high Hall-Petch slope of Mg-alloys [12,16–18] makes grain refinement very effective for simultaneous improvement of both strength and ductility; (3) a grain refined microstructure reduces deformation twinning and the formation of basal texture [14,15], promotes non-basal slip during thermal-mechanical processing [19,20], increases formability, and improves compression/tension yield anisotropy [21]; and (4) grain refinement also improves simultaneously the corrosion resistance [13], creep resistance [22] and fatigue strength [23,24] of Mg-alloys through finely dispersed and uniformly distributed second phase particles.

Grain refinement of Mg-alloys is currently achieved through two different approaches. One is the thermal-

* Corresponding author.
E-mail address: zhongyun.fan@brunel.ac.uk (Z. Fan).

https://doi.org/10.1016/j.jma.2022.10.006

mechanical treatment of solid Mg-alloys involving plastic deformation and dynamic recrystallization, such as severe plastic deformation (SPD) techniques [25–29]. For example, fine-grained, or even ultrafine- and nano-grained Mg-alloys can be obtained by friction stir processing (FSP) [30–32], equal-channel angular pressing (ECAP) [33–35], high-pressure torsion (HPT) [36,37]. The other is grain refinement during solidification processing either by chemical inoculation or through the application of external physical fields, such as ultrasonic treatment (UST) [38], electromagnetic stirring [39–41], and more recently intensive melt shearing [42–45]. Among these methods, chemical inoculation prior to the casting process has dominated the research effort [46–52]. Generally, chemical inoculation refers to the addition of grain refiners that contain both potent nucleant particles to promote heterogeneous nucleation and solute elements for growth restriction to enhance grain initiation. In this overview, we focus our attention on grain refining Mg-alloys by intensive melt shearing.

So far, Mg-Zr master alloys remain the only commercially available grain refiner for Mg-alloys. More than 80% of grain refinement is achieved through the addition of Mg-Zr grain refiners [48]. Unfortunately, Zr-containing grain refiners do not work for Mg-alloys containing Al, Si, and Mn [49,53], most likely due to the formation of intermetallic phases between Zr and such alloying elements. However, Mg-Al-based alloys constitute a major part of the Mg-alloys used in industries [3]. Extensive work has been dedicated to the search for effective, low cost and easy-to-use grain refiners for Mg alloys, especially for Mg-Al-based alloys (see the reviews in Refs. [48–54]).

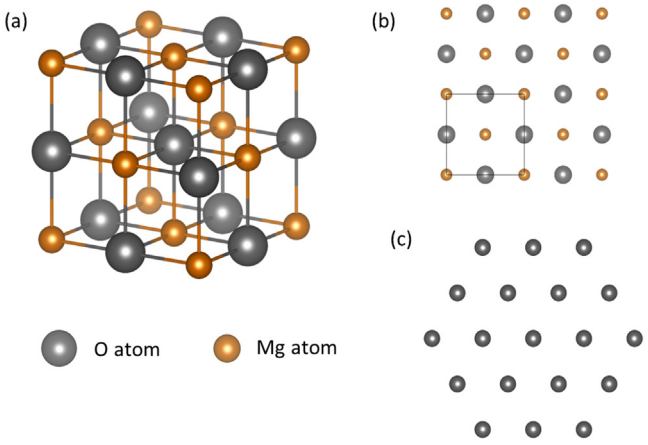

Fig. 1. Schematic illustration of the atomic arrangement of MgO. (a) The unit cell of fcc MgO; (b) atomic arrangement of the {0 0 1} terminated cubic MgO surface; and (c) atomic arrangement of the {1 1 1} oxygen terminated octahedral MgO surface.

In recent years, with significant support from the EPSRC (Engineering and Physical Science Research Council, UK), the LiME (liquid Metal Engineering) Research Hub [55] has focused its fundamental research on the early stage of solidification. Significant advances have been made in the understanding of prenucleation [56–62], heterogeneous nucleation [63–67], grain initiation [67–70] and their effect on grain

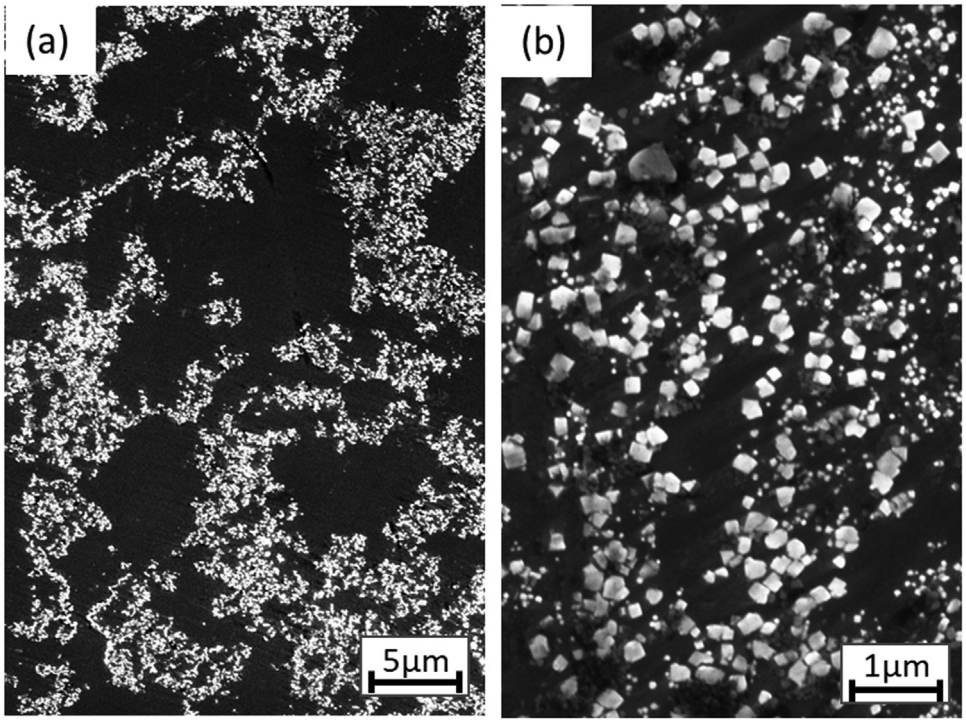

Fig. 2. Scanning electron microscopy (SEM) images of (a) MgO films and (b) MgO particles in an oxide film in commercial purity Mg (CP-Mg) melt [76], showing the general morphology of MgO films and MgO particles. The oxide films in the melt are liquid films that contain numerous discrete MgO particles.

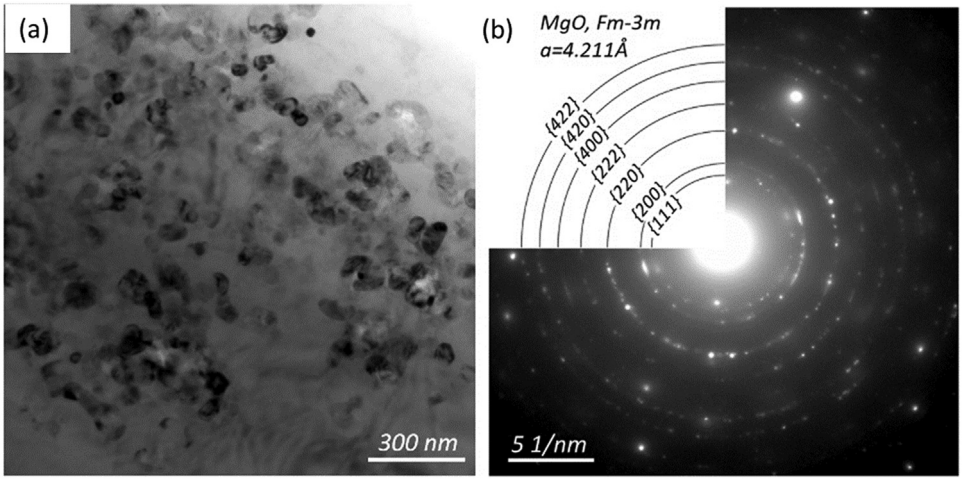

Fig. 3. (a) Bright-field transmission electron microscopy (TEM) image of an oxide film and (b) selected area electron diffraction (SAED) patterns taken from the oxide film in CP-Mg, showing the oxide film in CP-Mg consists of well-separated individual MgO particles [76].

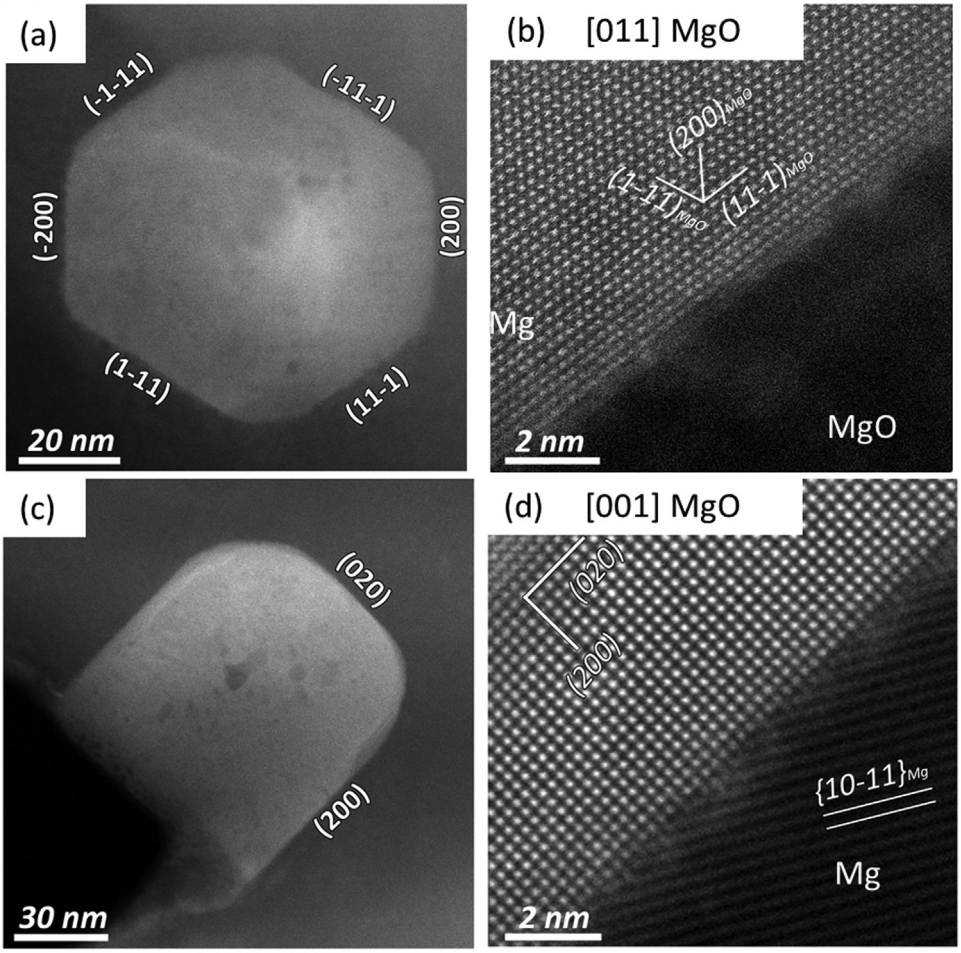

Fig. 4. Microscopic characterization of MgO particles [76]. (a, c) TEM images of {1 1 1} faceted octahedral MgO particle and {0 0 1} faceted cubic MgO particle; and (b, d) high resolution TEM (HRTEM) images of MgO{1 1 1} and MgO{0 0 1} viewed along [0 1 1] and [0 0 1] MgO directions, respectively, showing atomically sharp facets.

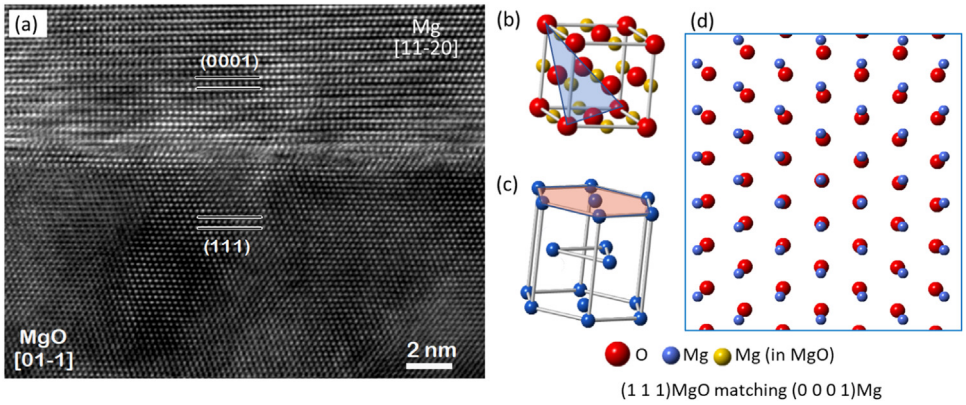

Fig. 5. Evidence of heterogeneous nucleation of Mg on a MgO{1 1 1} particle [43,76]. (a) HRTEM image showing the interface between (1 1 1)MgO and (0 0 0 1)Mg planes, indicating a well-defined orientation relationship (OR): OR1: (1 1 1) [0 1 $\bar{1}$]MgO // (0 0 0 1) [0 1 $\bar{2}$ 0]Mg; (b, c) schematics showing matching atomic planes of (b) (1 1 1)MgO and (c) (1 1 $\bar{2}$ 0)Mg in MgO and Mg unit cells, respectively; and (d) schematic showing the atomic configuration of the two matching planes along OR1, which indicates a large lattice misfit at (1 1 1)MgO/(1 1 $\bar{2}$ 0)Mg interface and thus a poor nucleation potency for MgO{1 1 1}.

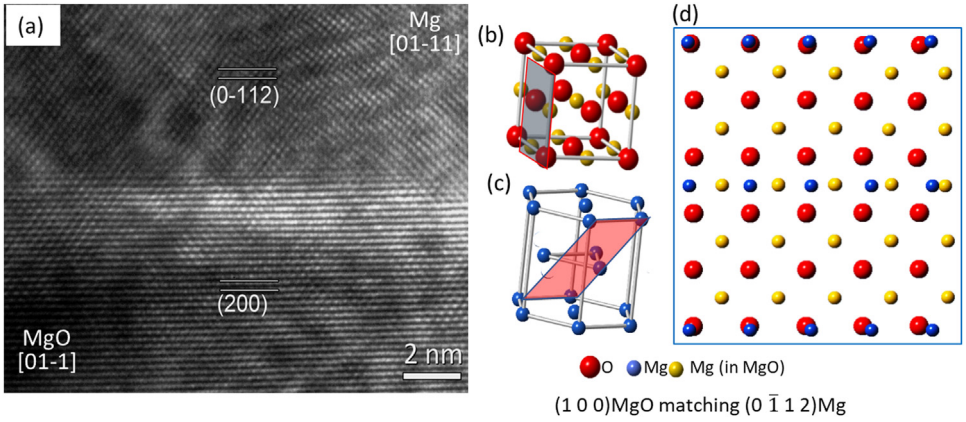

Fig. 6. Evidence of heterogeneous nucleation of α-Mg on a MgO{0 0 1} particle [76]. (a) HRTEM image showing the interface between (1 0 0)MgO and (0 $\bar{1}$ 1 2)Mg planes, indicating a well-defined orientation relationship (OR) between the two crystals: OR2: (2 0 0) [0 1 $\bar{1}$]MgO // (0 $\bar{1}$ 1 2) [0 1 $\bar{1}$ 1]Mg; (b, c) schematics showing matching atomic planes of (b) (1 0 0)MgO and (c) (0 $\bar{1}$ 1 2)Mg in MgO and Mg unit cells, respectively; and (d) schematic showing the atomic configuration of the two matching planes along OR2, which indicates a large lattice misfit at (1 0 0)MgO/(0 $\bar{1}$ 1 2)Mg interface and thus a poor nucleation potency for MgO{0 0 1}.

refinement [68–71]. This paper aims to provide a comprehensive overview of grain refinement of Mg-alloys by native MgO particles. We first present the physical and chemical nature of native MgO particles and their potential for grain refinement of Mg-alloys; this is followed by an overview of recent advances in understanding heterogeneous nucleation, grain initiation and their applications to industrial casting processes for grain refinement of Mg-alloys; and finally, we discuss the potential to make Mg-alloy self-grain-refining and the new approaches to the future development of refining Mg-alloys.

2. Native MgO in Mg-alloy melts

2.1. Nature of MgO crystal

Magnesia (MgO) has a NaCl-type structure (Fig. 1a), with a lattice parameter of $a = 4.2$ Å [72]. It is a typical ionic crystal and belongs to the family of MX (M represents a metallic element, X an element of high electronegativity). The ionic MgO crystals under ambient conditions have a stable {0 0 1} surface termination (denoted as MgO{0 0 1} hereafter), which contains equal numbers of the Mg^{2+} and O^{2-} ions (Fig. 1b) and therefore is non-polar [73]. A cleavage along the MgO <1 1 1> orientation produces two smooth surfaces: one with the Mg surface termination and the other with O surface termination (Fig. 1c), with both surfaces being polar. Such polar surfaces are unstable under ambient conditions but can be stabilized by defects, e.g. Mg or O domains [74]. However, the situation may become different when an ionic crystal is in contact with liquid metal. The free electrons of the liquid metal can eliminate the polar effect and stabilize the polar surfaces, such as in the case of MgO{1 1 1} in liquid Mg. MgO{1 1 1} surfaces have a 2-dimensional hexagonal lattice, which is similar to that of the close-packed Mg{0 0 0 1} plane.

Table 1
Calculated lattice misfit (f) between substrate/Al at 660 °C and substrate/Mg at 650 °C [44,68,76,78,80].

Substrate/Metal	Crustal structure, lattice constant at RT for substrate (nm)	Substrate surface termination	Orientation relationship (OR)	Lattice misfit f (%)	Refs.
TiB_2 / Al	hcp, a = 0.3030, c = 0.3229	(0 0 0 1)	(0 0 0 1)[1 1 -2 0] TiB_2 // (1 1 1)[0 -1 1] Al	-4.22	[80]
$TiB_2(Al_3Ti$ 2DC) / Al	Al_3Ti: tetragonal, a = 0.3848, c = 0.8596	(0 0 0 1)	(0 0 0 1)[1 1 -2 0] $TiB_2(Al_3Ti$ 2DC) // (1 1 1)[0 -1 1] Al	0.09	[80]
α-Al_2O_3 / Al	rhombohedral, a = 0.4759, c = 1.2993	(0 0 0 1)	(0 0 0 1)[1 0 -1 0]α-Al_2O_3 // (100)[001] Al	-0.48	[68]
γ-Al_2O_3 / Al	fcc, a = 0.7924	(1 1 1)	(1 1 1)[0 -1 1] γ-Al_2O_3 // (1 1 1)[0 -1 1] Al	3.38	[68]
$MgAl_2O_4$ / Al	fcc, a = 0.8083	(1 1 1)	(1 1 1)[1 1 0] $MgAl_2O_4$ // (1 1 1)[1 1 0] Al	1.4	[44]
MgO / Mg	fcc, a = 0.4211	(1 0 0)	(1 0 0)[0 -1 1] MgO // (0 -1 1 2)[0 1 -1 1] Mg	7.9	[76]
MgO / Mg	fcc, a = 0.4211	(1 1 1)	(1 1 1)[0 -1 1] MgO // (0 0 0 1)[1 1 -2 0] Mg	7.9	[76]
Zr / Mg	hcp, a = 0.3233, c = 0.5149	N/A	(0 0 0 1)[1 1 -2 0] Zr // (0 0 0 1)[1 1 -2 0] Mg	0.9	[78]

2.2. Oxide films in Mg-alloy melts

Oxide films play a critical role in determining the success of casting processes and the formation of cast defects which in turn affect the quality and performance of the final castings [75]. It is usually believed that oxide films, particularly those in Al-alloy melts, are solid films with a finite thickness, and appear in castings as double films with the dry sides facing each other, hence representing cracks in the solidified components [75].

Mg has a high affinity with oxygen, and oxide films form instantly on the melt surface freshly exposed to the ambient atmosphere during melting and melt handling, even though protective cover gas is used to prevent the melt from severe oxidation [76,77]. Using a pressurized melt filtration method [43,76,78,79], oxide films can be collected from various Mg-alloy melts to facilitate direct examination of the oxide films and particles. It has been confirmed that oxide films in Mg-alloy melts are of three distinctive types [43,76]:

- *Young oxide films*: They are formed through instantaneous oxidation of freshly exposed melt surfaces during melt handling, such as melt transfer and pouring. They have a thickness of 1–2 μm and appear in the liquid in a form of "wiggly worms" (Fig. 2a). Young oxide films are not solid films, but liquid films containing individual nano-sized MgO particles (Figs. 2b and 3) [76].
- *Old oxide films*: They are formed on the top of the alloy melt in the crucible during melting through sustained oxidation for a long period of time. Due to the use of protective gas on top of the melt, old oxide films often contain S and F. Old oxide films usually have a thickness of 5–10 μm, a "cauliflower" morphology and are continuous by nature [43,76].
- *Ingot skins*: They are brought into the alloy melt from the original Mg-alloy ingot. Ingot skins appear in the melt as straight segments that consist of discrete MgO particles (nano-size) well dispersed in the Mg matrix [43].

Among the three types of oxide films, young oxide films are dominant in numbers in the alloy melt. The number of old oxide films can be reduced by appropriate de-drossing operations prior to metal casting. Entrained old oxide films in alloy melts are rare events. Similarly, ingot skins are also rare events in alloy melt. Our studies have been focusing on the nature of young oxide films and their effects on the grain refinement of Mg-alloys [43,76].

2.3. Morphology of native MgO

Native MgO particles in Mg melts are faceted crystals and have two distinctive morphologies: one is {1 1 1} terminated octahedral (often truncated) and denoted as MgO{1 1 1} hereafter (Fig. 4a); and the other is {0 0 1} terminated cubic and denoted as MgO{0 0 1} hereafter (Fig. 4c) [76]. Like many other cubic crystals, fcc MgO grows fast along with its <0 0 1> directions and leaves the slowly growing {1 1 1} planes as the terminating surfaces, giving rise to a truncated octahedral morphology. The transmission electron microscopy (TEM) images in Fig. 4a and c show the detailed surface termination of MgO particles collected from Mg-alloy melts, and the high-resolution transmission electron microscopy (HRTEM) images in Fig. 4b and d show the atomically sharp facets of MgO{1 1 1} and MgO{0 0 1} viewed along [0 1 1] and [0 0 1] MgO directions, respectively. Fig. 4 suggests that both MgO{1 1 1} and MgO{0 0 1} particles usually have clean terminating surfaces that are free from any contamination by adsorption of alloying and impurity elements.

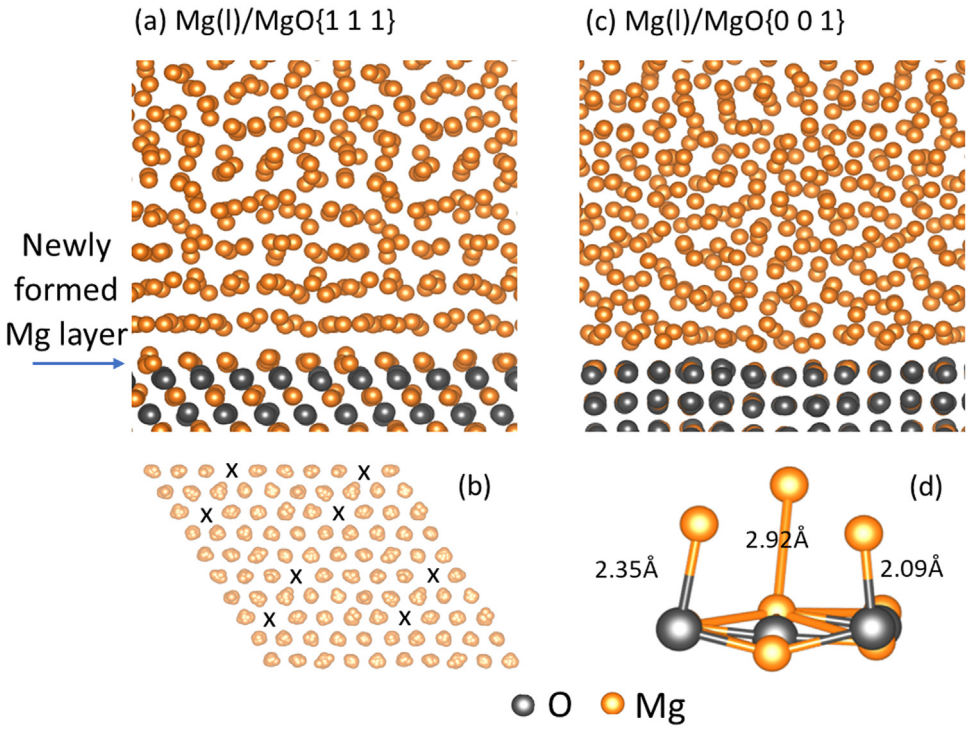

Fig. 7. *Ab initio* MD simulations for Mg(*l*)/MgO interfaces [59]. (a) Mg(*l*)/MgO{1 1 1} and (c) Mg(*l*)/MgO{0 0 1} interfaces, showing atomically rough; (b) the first liquid Mg layer induced by the usually O-terminated MgO{1 1 1} substrate, containing vacancies as marked by the "x"; and (d) the first liquid Mg layer induced by the MgO{0 0 1} substrate, showing atomically rough surface due to the varying bond lengths between liquid Mg atoms and the O^{2-} and Mg^{2+} ions on the MgO{0 0 1} surface.

It has been suggested that the octahedral MgO{1 1 1} particles are formed by oxidation of liquid Mg on the freshly exposed Mg melt surface, while the cubic MgO{0 0 1} particles are a product of oxidation of Mg vapour above the Mg melt surface and reintroduced subsequently into the alloy melt [76].

2.4. Heterogeneous nucleation of Mg on native MgO

Direct evidence for heterogeneous nucleation of Mg on native MgO particles with well-defined orientation relationships (ORs) between Mg and MgO is repeatedly observed by HRTEM [43,76,78,79]. Fig. 5 shows an example of Mg solid nucleated on the (1 1 1) surface of an octahedral MgO particle [43,76] with the following OR:

$$\mathrm{OR1}: (1\,1\,1)\left[0\,1\,\bar{1}\right]\mathrm{MgO}//(0\,0\,0\,1)\left[1\,1\,\bar{2}\,0\right]\mathrm{Mg}. \quad (1)$$

The TEM image in Fig. 5a shows the sharp interface between MgO and Mg being viewed along [0 1 $\bar{1}$]MgO and [1 1 $\bar{2}$ 0]Mg directions and the schematics in Fig. 5b and c illustrate the matching atomic planes of (1 1 1)MgO and (0 0 0 1)Mg in the MgO and Mg unit cells, respectively. Fig. 5d shows the atomic matching of the two planes, indicating a relatively poor matching between surface O atoms (red spheres) of MgO and Mg atoms (blue spheres) of Mg at the interface, despite the same hexagonal atomic arrangement in the two planes. The calculated lattice misfit is 7.9% according to the lattice parameters of MgO and Mg at 650 °C [76], being much larger than 0.09%, the lattice misfit between the extremely potent TiB_2/Al_3Ti-2DC (2-dimensional compound) and Al [80], suggesting a low potency of the native MgO{1 1 1} particles for nucleating Mg.

The MgO{1 0 0} particles are also found to nucleate Mg on its {1 0 0} terminating surfaces with a well-defined OR between the two crystals (Fig. 6a) [76,81]:

$$\mathrm{OR2}: (2\,0\,0)\left[0\,1\,\bar{1}\right]\mathrm{MgO}//\left(0\,\bar{1}\,1\,2\right)\left[0\,1\,\bar{1}\,1\right]\mathrm{Mg}. \quad (2)$$

Fig. 6b and c schematically show (2 0 0) MgO and (0 $\bar{1}$ 1 2) Mg planes in their respective unit cells, and Fig. 6d shows the atomic configuration in the two matching planes. According to OR2, the calculated lattice misfit at the (1 0 0)MgO/Mg interface is 7.9% [76], being the same as that at the MgO{1 1 1}/Mg interface.

Generally, lattice misfit (*f*) between the substrate (N) and the solid (S) can only be defined for a specified OR between the two crystals [63]:

$$(h\ k\ l)[u\ v\ w]_N//\left(h'\ k'\ l'\right)\left[u'\ v'\ w'\right]_S, \quad (3)$$

$$f = \frac{d_{[u'v'w']S} - d_{[uvw]N}}{d_{[u'v'w']S}} \times 100\%, \quad (4)$$

where $d_{[uvw]_N}$ and $d_{[u'v'w']_S}$ are the atomic spacings along the [u v w]$_N$ and [u′ v′ w′]$_S$ directions of the substrate and the solid, respectively. Table 1 lists the calculated lattice misfit values of some commonly encountered nucleation systems in Mg- and Al-alloys [44,68,76,78,80]. The calculated lattice

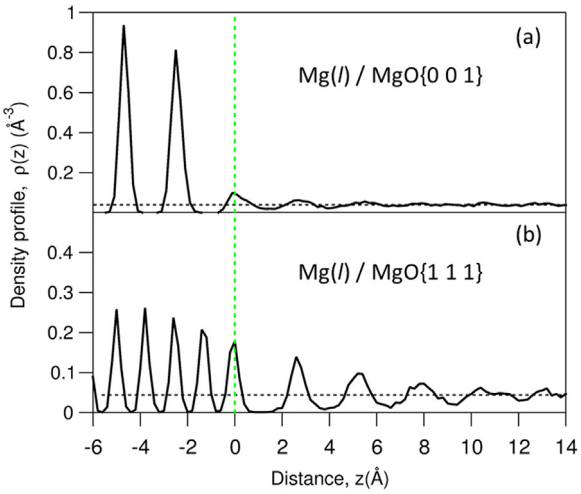

Fig. 8. Atomic density profiles across the (a) Mg(*l*)/MgO{0 0 1} and (b) Mg(*l*)/MgO{1 1 1} interfaces showing the significantly reduced atomic layering at the interface, particular at the Mg(*l*)/MgO{0 0 1} interface [59].

misfit (7.9%) for both MgO{1 1 1}/Mg and MgO{1 0 0}/Mg systems is much larger than those for other substrate/metal systems. Such a large lattice misfit suggests a poor nucleation potency of both MgO{1 1 1} and MgO{1 0 0} as the substrate for nucleating Mg.

2.5. Atomic arrangement at the Mg(l)/MgO(s) interface

Ab initio molecular dynamics (MD) simulation was used to assess the interaction between the terminating MgO surface and liquid Mg and the resultant atomic arrangement at the Mg(*l*)/MgO(*s*) interfaces [59]. It is revealed that, upon thermal equilibrium being reached, a new Mg layer formed on the surface of MgO{1 1 1}, regardless of the initial surface termination of MgO{1 1 1} with either O or Mg. Fig. 7a presents a snapshot of the simulation system equilibrated at 1000 K (front view) showing the newly formed terminating Mg layer on the MgO{1 1 1} surface and some degree of atomic layering in the liquid adjacent to the interface. Fig. 7b is a top view of the atomic arrangement of the newly formed terminating Mg layer on the MgO{1 1 1} surface revealed by the time-averaged atomic positions. The existence of vacancies in the layer as marked by "x" makes the MgO{1 1 1} surface atomically rough and thus reduces the potency of MgO{1 1 1} as a substrate for nucleating Mg.

Similarly, Fig. 7c shows a snapshot of the Mg(*l*)/MgO{0 0 1} system equilibrated at 1000 K (front view) showing the atomic arrangement across the interface. Fig. 7d shows the nature of chemical bonding between different atoms across the Mg(*l*)/MgO{0 0 1} interface under equilibrium conditions. The bond length between the Mg^{2+} ion in the MgO{1 0 0} surface and the Mg atom in the melt is 2.92 Å, 0.8 Å longer than that between the O^{2-} ion and Mg atom in the melt (Fig. 8d), and thus the surface of MgO{1 0 0} is atomically rough [59]. Consequently, the ability of MgO (1 0 0) to template atomic ordering in the melt is significantly reduced [59]. As shown in Fig. 8, the number of atomic layers in both interfaces is less than 6, the atomic layers in an interface with a smooth substrate surface. It is also noted that atomic layering at the Mg(*l*)/MgO{1 1 1} interface (Fig. 8b) is more pronounced than that at the Mg(*l*)/MgO{0 0 1} interface (Fig. 8a).

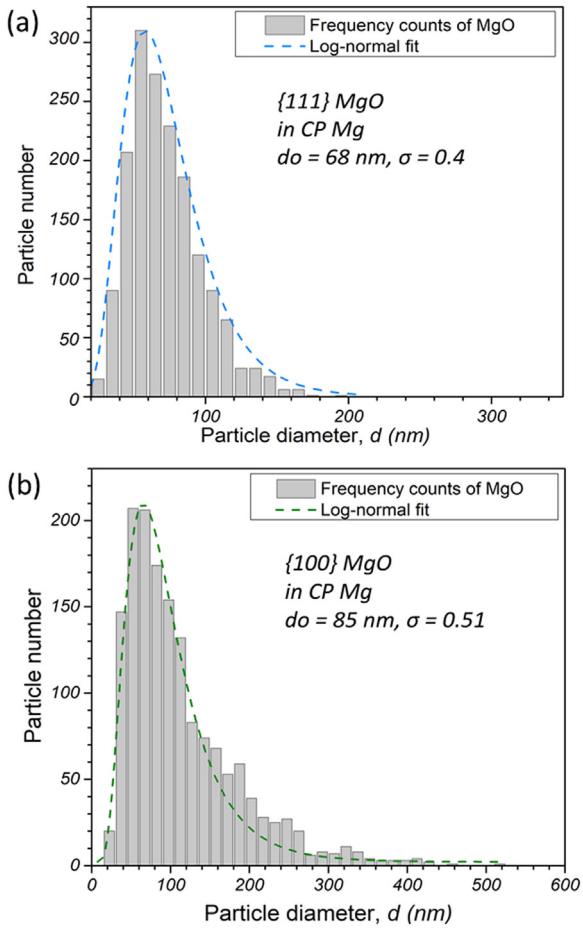

Fig. 9. Statistical quantification of the size of two morphologies of MgO particles in CP-Mg, showing that both two types of native MgO particles have a log-normal size distribution [76]. (a) MgO {1 1 1} and (b) MgO {1 0 0}.

2.6. Particle size and size distribution of MgO particles in Mg-alloy melt

Native MgO particles have two different morphologies in Mg-alloys: MgO{1 1 1} and MgO{0 0 1} [76]. Although these two types of MgO particles are formed by different mechanisms, their sizes follow the log-normal distribution [76,82]:

$$\frac{dN}{dd} = \frac{N_0}{\sigma d\sqrt{2\pi}} \exp -\left(\frac{[\ln(d) - \ln(d_0)]^2}{2\sigma^2}\right), \quad (5)$$

where d_0 is the geometric mean of particle diameters, N_0 is the total particle number and σ is the standard deviation.

As shown in Fig. 9, the fitted d_0 of native MgO particles is 0.068 and 0.085 μm with a similar size spreading

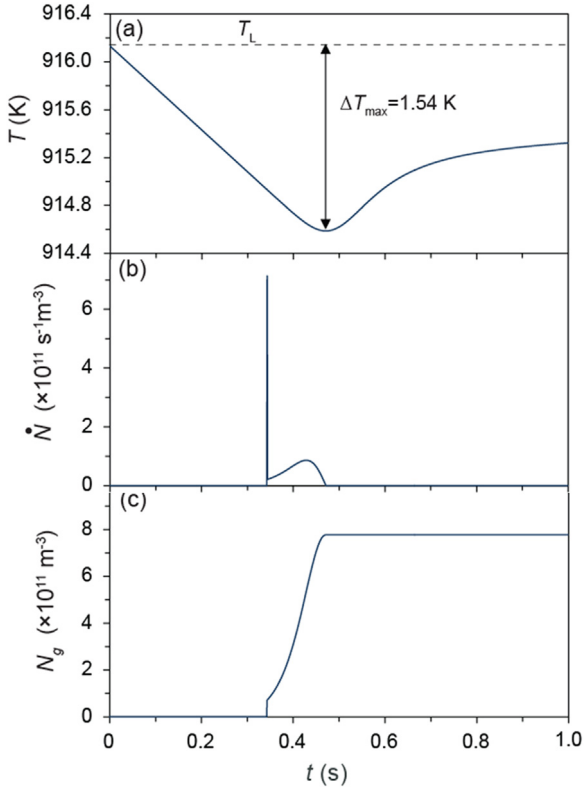

Fig. 10. Solidification behaviour of Mg-1Al alloy without intensive melt shearing at $\dot{T}$ = 3.5 K/s. (a) cooling curve, (b) grain initiation rate, and (c) total grain initiation events. Native oxide particles are assumed to have a nucleation undercooling (ΔT_n) of 1.2 K, with a number density of 10^{14} m^{-3} (non-sheared) and a log-normal size distribution (d_0 = 0.07 μm, σ = 0.45). The grain initiation occurs initially by EGI (9.2% of the total), followed by PGI (90.8% of the total).

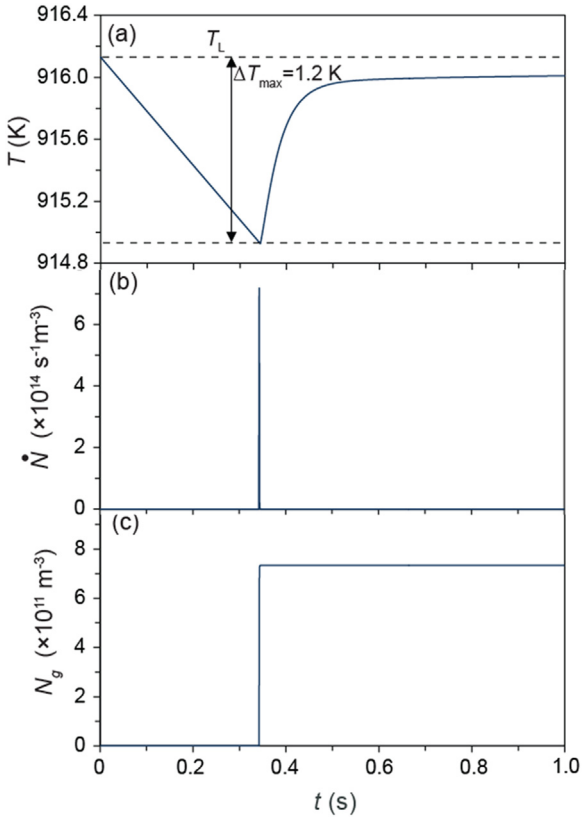

Fig. 11. Solidification behaviour of Mg-1Al alloy with intensive melt shearing at $\dot{T}$ = 3.5 K/s. (a) cooling curve, (b) grain initiation rate, and (c) total grain initiation events. Native oxide particles are assumed to have a nucleation undercooling (ΔT_n) of 1.2 K, with a number density of 10^{17} m^{-3} (sheared) and a log-normal size distribution (d_0 = 0.07 μm, σ = 0.45). The grain initiation is fully explosive.

(σ is 0.40 and 0.51) for the MgO{1 1 1} and MgO{1 0 0} particles, respectively [76], which is consistent with previous result (d_0 = 0.07 μm and σ = 0.45) [82] where the MgO{1 1 1} and MgO{1 0 0} were not distinguished during measurement. The size of native MgO particles is much smaller than that of the particles in other grain refiners. For example, the d_0 of native MgO is one order of magnitude smaller than that of TiB_2 particles in commercial Al-5Ti-1B grain refiner for Al-alloys (0.68 μm [83]). More importantly, the number density of the native MgO particles in Mg-alloys is found to be 10^{17} m^{-3} in the intensively sheared Mg melts [82], a few orders of magnitude higher than that of TiB_2 particles in Al-alloys with 1 ppt (0.1 wt.%) Al-5Ti-1B grain refiner addition ($\sim 10^{13}$ m^{-3} [83]).

2.7. The potency of native MgO for nucleating Mg

From the previous analysis, we understand that both MgO{1 1 1} and MgO{0 0 1} particles have a 7.9% lattice misfit with Mg [76], which is considerably larger than those for the commonly encountered grain refiner systems (see Table 1). In addition, our density functional theory (DFT) calculation [59] suggests that both MgO{1 1 1} and MgO{0 0 1} have atomically rough surfaces due to their interaction with molten Mg (Fig. 7). The large lattice misfit and atomically rough terminating surfaces make both MgO{1 1 1} and MgO{0 0 1} particles poor substrates for templating atomic ordering at the Mg(*l*)/MgO(*s*) interfaces at both prenucleation and heterogeneous nucleation stages (Fig. 8). Therefore, it can be concluded that both MgO{1 1 1} and MgO{0 0 1} are highly impotent for heterogeneous nucleation of Mg compared with TiB_2 with Al_3Ti 2DC for Al.

3. Grain refinement of Mg-alloys by native MgO

3.1. Native MgO is the only type of solid particle of significance in Mg-melts

Due to the high oxidation potential of Mg, molten magnesium oxidises readily and rapidly when it is in contact with air, resulting in inclusion contents 10–20 times higher than that in Al (0.1–10 ppm for pure Al, 10–200 ppm for pure Mg) [84,85]. During the melting and casting processes, magnesium oxide (MgO) and magnesium nitrides (Mg_3N_2) are formed due to the reaction of molten Mg with oxygen and nitrogen in the atmosphere. The Mg_3N_2 inclusions appear often together with oxide clusters or films [85,86]. Besides MgO and Mg_3N_2, some other inclusions, such as MgS and MgF_2,

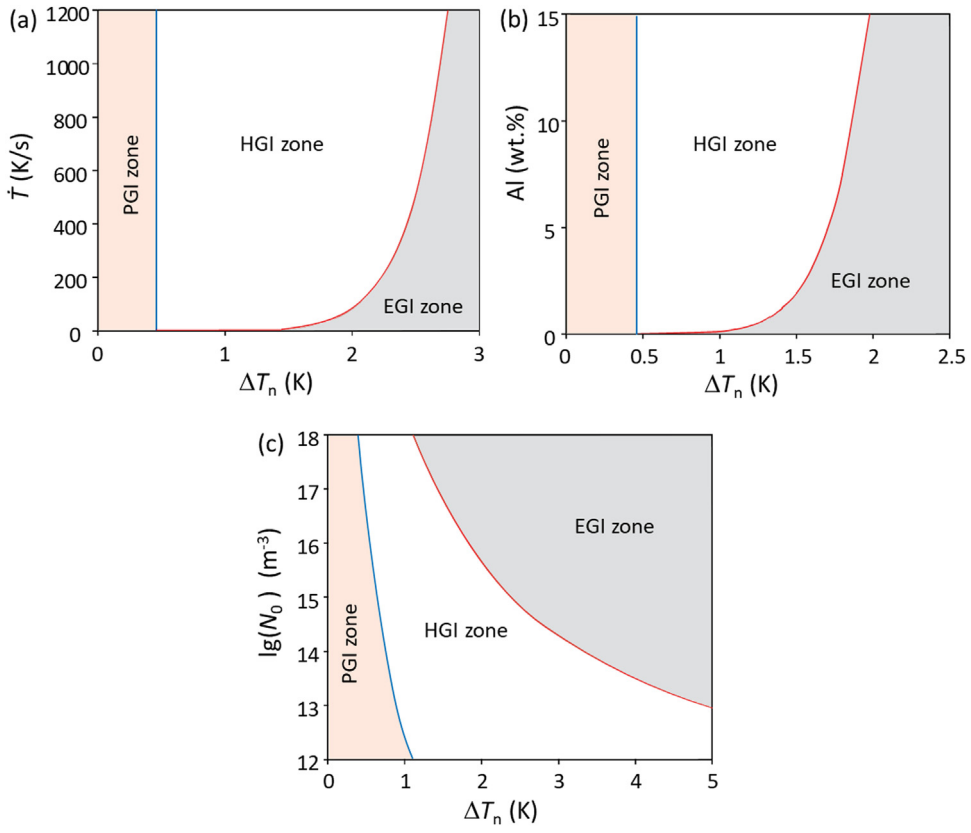

Fig. 12. Grain initiation maps for Mg-Al alloys containing nucleant particles which have a varying nucleation potency but constant log-normal particle size distribution [69,70]. (a) Grain initiation map ($\Delta T_n - \dot{T}$ plot) for Mg-1Al alloy with $N_0 = 10^{17}$ m^{-3} showing the effect of cooling rate ($\dot{T}$) on grain initiation behaviour; (b) grain initiation map ($\Delta T_n - C_0$ plot) for Mg-Al alloys with $N_0 = 10^{17}$ m^{-3} and $\dot{T} = 3.5$ K/s showing the effect of solute concentration (C_0) on grain initiation behaviour; (c) grain initiation map ($\Delta T_n - \lg(N_0)$ plot) for Mg-1Al alloy at $\dot{T} = 3.5$ K/s showing the effect of particle number density (N_0) on grain initiation behaviour. The solid blue line marks the limit for progressive grain initiation ($\Delta T_n = \Delta T_{gi}(1st)$) and the solid red line marks the limit for explosive grain initiation ($\Delta T_n = \Delta T_{max}$). These two lines divide the grain initiation map into 3 distinct zones: progressive grain initiation (PGI) zone where $\Delta T_n < \Delta T_{gi}(1st)$; explosive grain initiation (EGI) zone where $\Delta T_n = \Delta T_{max}$; and the hybrid grain initiation (HGI) zone where $\Delta T_{gi}(1st) \leq \Delta T_n < \Delta T_{max}$.

may also form by the reaction of molten Mg with protective gases during the melting process [85,86]. However, among these inclusions, the MgO particles are the dominant inclusions in Mg-alloys with a number density as high as 10^{17} m^{-3}, which is much higher than that of other inclusions. Although other inclusion particles may participate in heterogeneous nucleation and even grain initiation, their existence will alter neither the general features of solidification nor the final grain size due to their low number density in Mg-melts. Therefore, we can conclude that native MgO is the only type of particle of significance in Mg-alloy melts in terms of grain refinement. As will be discussed further later, this provides us with a great opportunity for effective grain refinement of Mg-alloys without the need for the addition of any grain refiners.

3.2. Solidification behaviour of Mg-alloys

For Mg-alloys without inoculation, the native MgO particles are the most likely substrates for heterogeneous nucleation and dominate the subsequent grain initiation process during solidification [43]. In this section, we will use a numerical approach to demonstrate the solidification behaviour of Mg-alloys under different conditions. The details of the numerical model and parameters used in this paper can be found elsewhere [69]. Here we present some of the key parameters used during our calculations for quick reference: the MgO particle number densities (N_0) are 10^{14} and 10^{17} m^{-3} for Mg-alloys without and with intensive melt shearing, respectively [82]; the MgO particle size distribution follows the same log-normal distribution ($d_0 = 0.07$ μm, $\sigma = 0.45$) for all Mg-alloys [82]; the nucleation undercooling (ΔT_n) for MgO is estimated to be 1.2 K [69], reflecting the low nucleation potency of MgO for Mg; and the cooling rate ($\dot{T}$) is 3.5 K/s corresponding to that for the standard TP-1 test [87].

Recently, Fan and co-workers [68–70] identified two distinctive grain initiation modes depending on the interplay between nucleation undercooling (ΔT_n) and grain initiation undercooling of the largest nucleant particle ($\Delta T_{gi}(1st)$): progressive grain initiation (PGI) and explosive grain initiation (EGI), which divide the grain initiation behaviour into three zones: a PGI zone, an EGI zone and a hybrid grain initiation (HGI) zone [69,70]. PGI is defined as a grain initiation process which starts with the largest solid particle(s) and continues with the progressively smaller ones and finishes at recalescence. A necessary condition for PGI is $\Delta T_n < \Delta T_{gi}(1st)$, i.e., heterogeneous nucleation takes place on all

nucleant particles before any grain initiation events. Meanwhile, EGI is defined as a grain initiation process, in which a group of solid particles initiate grains almost simultaneously and the latent heat released by both heterogeneous nucleation and the initial free growth can cause an immediate recoalescence which stifles any further grain initiations [69,70]. A necessary condition for EGI is $\Delta T_n \approx \Delta T_{max}$, where ΔT_{max} is the undercooling at recalescence. The HGI is a combination of the initial EGI followed by PGI. A necessary condition for HGI is $\Delta T_{gi}(1st) < \Delta T_n < \Delta T_{max}$.

The calculated cooling curve of Mg-1Al alloy without intensive melt shearing is shown in Fig. 10a, where the maximum undercooling (ΔT_{max}) is 1.54 K, and the temperature increases gradually after recalescence. The largest MgO particle, $d(1st)$, is 0.78 μm, which corresponds to a grain initiation undercooling, "$\Delta T_{gi}(1st)$" = 0.76 K. Therefore, this satisfies "$\Delta T_{gi}(1st)$" (0.76 K) < ΔT_n < ΔT_{max} (1.54 K), and the grain initiation is HGI, as shown by the evolution of grain initiation rate (i.e., number of grain initiation events per unit time and per unit volume) during solidification (Fig. 10b). Please note that "$\Delta T_{gi}(1st)$" would be the undercooling required for the largest solid particles to initiate grains if heterogeneous nucleation has occurred. When Mg-1Al alloy solidifies at an undercooling (ΔT) of 0.76 K, there is no grain initiation since MgO particles need to nucleate Mg at large undercooling (ΔT_n = 1.2 K). After nucleation at $\Delta T = \Delta T_n$, a population of the solid particles (7.136×10^8 m^{-3}) satisfy the grain initiation criterion and initiate grains simultaneously in an EGI manner. However, the heat released by the growth of the initiated grains is not enough to cause recalescence and the system can continue to cool to a lower temperature, which makes it possible for the smaller solid particles to initiate grains. After EGI, further grain initiations occur progressively to smaller solid particles in a PGI manner until recalescence, which stifles any further grain initiation (Fig. 10b). The calculated average grain size is 400 μm, and the number of grains formed by EGI is 9.2% of the total grains (Fig. 10c), being less than 50%. This suggests that the solidification of Mg-1Al alloy without intensive melt shearing at a cooling rate of 3.5 K/s is PGI dominant.

Fig. 11a shows the calculated cooling curve of Mg-1Al alloy with intensive melt shearing, where the calculated ΔT_{max} is 1.2 K and the temperature increases sharply after recalescence. With intensive melt shearing, MgO particle number density (N_0) increases from 10^{14} to 10^{17} m^{-3} [82], and the largest MgO particle, $d(1st)$, is now 1.28 μm, which corresponds to the grain initiation undercooling, "$\Delta T_{gi}(1st)$" = 0.46 K. As the first grain initiation must start after nucleation, we have: $\Delta T_{gi}(1st) = \Delta T_n \approx \Delta T_{max} = \Delta T_{gi}(L^{st})$, and the grain initiation takes place in an extremely short period of time (Fig. 11b and c), which is a typical case for EGI. The grain initiation rate only has one very sharp peak during solidification (Fig. 11b). The calculated grain size is 88 μm, suggesting that intensive melt shearing can lead to significant grain refinement due to the promotion of explosive grain initiation.

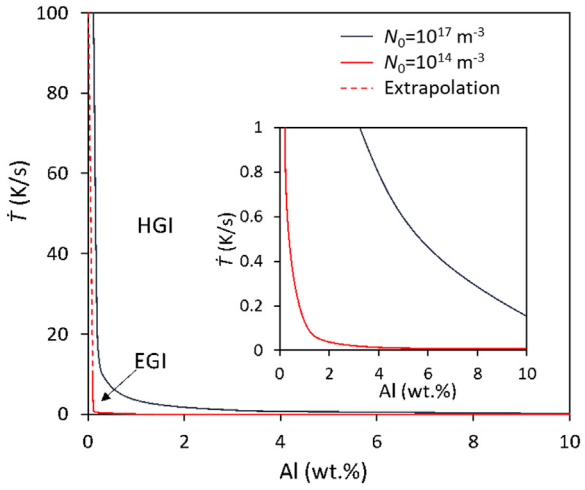

Fig. 13. Grain initiation map for Mg-Al alloys without and with intensive melt shearing, corresponding to MgO particle number density N_0 = 10^{14} and 10^{17} m^{-3}, respectively. Native oxide particles are assumed to have a nucleation undercooling (ΔT_n) of 1.2 K and a log-normal size distribution (d_0 = 0.07 μm, σ = 0.45). Under such conditions, it is impossible to have fully progressive grain initiation. The solid black line represents the bounder between EGI and HGI for $N_0 = 10^{17}$ m^{-3} and the solid red line for $N_0 = 10^{14}$ m^{-3}. The dashed red line is an extrapolation of the solid red line. The inset shows the enlarged region of the bottom-left corner of the diagram.

As discussed previously, PGI requires $\Delta T_n < \Delta T_{gi}(1st)$, i.e., heterogeneous nucleation must take place before any potential grain initiation events. For Mg-alloys with native MgO particles, ΔT_n = 1.2 K. A complete PGI thus requires that no MgO particles are greater than 490 nm in size, which is not practically possible. Therefore, there will be impossible for any Mg-alloy to solidify in a completely PGI manner.

3.3. Grain initiation maps

The grain initiation behaviour during the solidification of Mg-alloy is determined by the following factors: cooling rate ($\dot{T}$), solute concentration (C_0), nucleation potency (ΔT_n) and particle number density (N_0). The grain initiation behaviour can be conveniently presented by the grain initiation maps [69,70]. Fig. 12 demonstrates the grain initiation maps for Mg-Al alloys in the forms of ΔT_n-$\dot{T}$, ΔT_n-C_0 and ΔT_n-N_0 plots to illustrate the effects of cooling rate, solute concentration and particle number density on grain initiation behaviour [69,70]. In Fig. 12 there are two different types of solid lines: the blue lines represent $\Delta T_n = \Delta T_{gi}(1st)$ and the red lines $\Delta T_n = \Delta T_{gi}(L^{st}) = \Delta T_{max}$. They divide each plot into 3 distinct zones: a progressive zone, an explosive zone and a hybrid zone, corresponding to PGI, EGI, and HGI behaviour for grain initiation [69,70].

For Mg-alloys with native MgO particles (ΔT_n = 1.2 K), the grain initiation behaviour is affected by $\dot{T}$, C_0 and N_0. Fig. 13 shows the grain initiation maps in the form of $\dot{T}$ - C_0 plot for Mg-Al alloys without and with intensive melt shearing, corresponding to N_0 = 10^{14} and 10^{17} m^{-3}, respectively. As shown in Section 3.2, we have $\Delta T_n > \Delta T_{gi}(1st)$ with and without intensive melt shearing, suggesting that there is

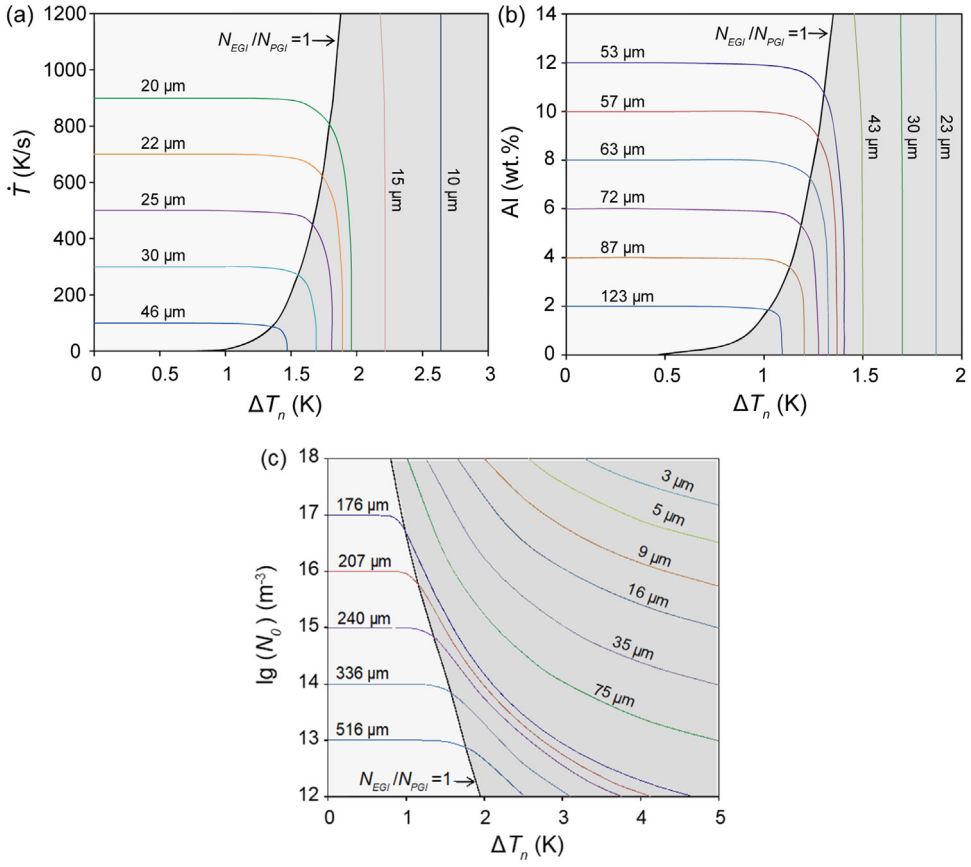

Fig. 14. Grain refinement maps for Mg-Al alloys containing nucleant particles with varying nucleation potency but constant log-normal particle size distribution [69,70]. (a) Grain refinement map ($\Delta T_n - \dot{T}$ plot) for Mg-1Al alloy with $N_0 = 10^{17}$ m^{-3} showing the effect of cooling rate on grain refinement; (b) grain initiation map ($\Delta T_n - C_0$ plot) for Mg-Al alloys with $N_0 = 10^{17}$ m^{-3} and $\dot{T} = 3.5$ K/s showing the effect of solute concentration on grain refinement; (c) grain initiation map ($\Delta T_n - lg(N_0)$ plot) for Mg-1Al alloy at $\dot{T} = 3.5$ K/s showing the effect of particle number density on grain refinement. The solid black line represents the conditions where explosive grain initiation has equal proportion with progressive grain initiation (N_{EGI}:$N_{PGI} = 1$); the light and dark grey coloured zones mark PGI-dominant and EGI-dominant zones, respectively. The thin coloured lines are iso-grain-size lines with the grain size being attached to each iso-grain-size line.

no fully PGI during the solidification of Mg-Al alloys. The red and black lines represent the boundaries between EGI and HGI for $N_0 = 10^{14}$ and 10^{17} m^{-3}, respectively. The red dashed line is an extrapolation of the red line because in this low C_0 range the freezing range is smaller than ΔT_n, suggesting that solidification may become partitionless [88]. From Figs. 12 and 13, it is clear that EGI is favoured by a slower cooling rate, lower solute concentration, lower nucleation potency and a larger particle number density. In addition, it should be pointed out that EGI may not necessarily result in grain refinement. For example, the grain initiation in Mg-1Al and Mg-9Al alloys with intensive melt shearing is EGI and HGI, respectively. However, the grain size of Mg-1Al alloy (88 μm) is larger than that of Mg-9Al alloy (59 μm).

3.4. Grain refinement maps

To understand the effect of grain initiation behaviour on grain refinement, the concept of the grain refinement map has been developed [69,70]. The effects of nucleation potency, cooling rate, solute concentration and particle number density on the grain size of Mg-Al alloys are shown by the iso-grain-size lines in Fig. 14. In Fig. 14 the solid black lines represent N_{EGI}:$N_{PGI} = 1$, which delineates the PGI-dominant zone ($N_{PGI} > N_{EGI}$) from the EGI-dominant zone ($N_{PGI} < N_{EGI}$), where N_{PGI} and N_{EGI} are the total numbers of PGI and EGI events during solidification, respectively.

Cooling rate and solute concentration have a similar trend on grain size (Fig. 14a and b). In the PGI-dominant zone, grain size decreases with increasing cooling rate and solute concentration but is almost independent of ΔT_n for a given cooling rate and solute concentration; whilst in the EGI-dominant zone, grain size decreases with increasing ΔT_n, but is almost independent of cooling rate and solute concentration for a given ΔT_n. However, for a given ΔT_n, the grain size decreases with increasing particle number density in both PGI-dominant and EGI-dominant zones (Fig. 14c), but with different efficiency: in the PGI-dominant zone, grain size decreases moderately with increasing N_0 and is independent of ΔT_n; whilst in the EGI-dominant zone, grain size not only decreases more rapidly with increasing N_0 but also decreases with increasing ΔT_n.

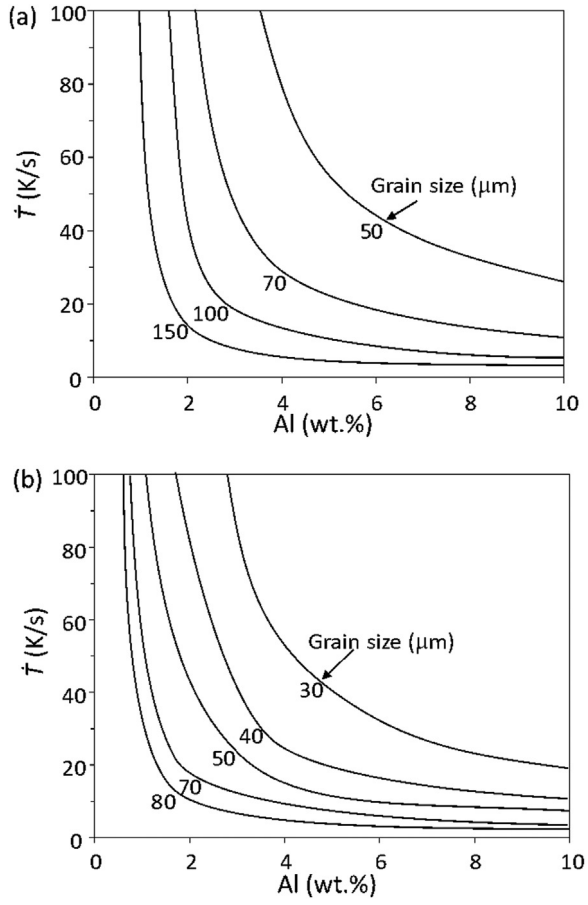

Fig. 15. Grain refinement maps for Mg-1Al alloy under different conditions. (a) Without intensive melt shearing ($N_0 = 10^{14}$ m^{-3}); and (b) with intensive melt shearing ($N_0 = 10^{17}$ m^{-3}). Native oxide particles are assumed to have a nucleation undercooling (ΔT_n) of 1.2 K and a log-normal size distribution ($d_0 = 0.07$ μm, $\sigma = 0.45$). The curves represent iso-grain-size lines with specific grain sizes as labeled by the data attached to each curve.

From the grain refinement maps (Fig. 14) we can conclude that for a specified Mg-alloy (fixed C_0) and a given solidification condition (fixed $\dot{T}$), grain refinement cannot be achieved by inoculation with more potent nucleant particles than MgO. In practical terms, this means that it is impossible to develop a grain refiner containing more potent particles than MgO, which can be more effective than the native MgO particles. In this case, further grain size reduction can only be made possible by increasing the MgO particle number density (e.g. intensive melt shearing) or by making the native MgO particles more impotent.

For Mg-alloys with native MgO particles ($\Delta T_n = 1.2$ K), the grain refinement maps for Mg-Al alloys without and with intensive melt shearing are shown in Fig. 15 in the form of the $\dot{T}$ - C_0 plot. Fig. 15 suggests that intensive melt shearing can significantly reduce the grain size of Mg-Al alloys with the same solidification process (constant cooling rate).

Although it is theoretically feasible to develop grain refiners for Mg-alloys with more impotent particles than MgO if MgO particles can be completely removed from the melt, it is practically very difficult to do so since: (1) the terminating surface of MgO not only has a large lattice misfit with Mg (7.9%) but also is atomically rough due to the presence of vacancies and vertical displacement of surface atoms. It will be very difficult to find the particles that are more impotent than MgO; (2) complete removal of MgO particles from Mg melt is almost impossible due to the high affinity of Mg to oxygen.

3.5. Experimental validation of theoretical calculations

In order to validate the theoretical predictions, a series of experiments have been carried out on Mg-Al alloys. The detailed experimental procedures were presented elsewhere [89,90]. In this section, we briefly sum up some of the key features of our experiments to ensure the reliability of our experimental findings:

(1) *Applying intensive melt shearing* [43,90]. The same experimental conditions for intensive melt shearing were applied to all the experiments to ensure the MgO particle number density is consistent in all the samples (approximately 10^{17} m^{-3} [82]).
(2) *Using a standard TP-1 test* [87,90]. The standard Alcan TP-1 test provides a quasi-isothermal solidification at a constant cooling rate (close to 3.5 K/s for Al-alloys) at the centre of the sample for Mg-alloys. Adaptation of TP-1 test procedures ensures the consistency of solidification conditions.
(3) *Checking microstructure on both vertical-section and cross-section* [71,89,90]. This ensures that grain size is measured only for equiaxed grain structures, avoiding the inaccuracy introduced by the "grain size" data measured from the columnar structures.

The optical macrographs in Fig. 16 show the grain structures of commercial purity Mg (CP-Mg) on both cross-section and vertical-section with and without intensive melt shearing. Without intensive melt shearing, CP-Mg has a fully columnar grain structure (Fig. 16a and c), while with intensive melt shearing the grain structure becomes fine and fully equiaxed (Fig. 16b and d). This result supports the conclusion from Figs. 13–15 that increasing nucleant particle number density promotes explosive grain initiation and leads to significant grain refinement. In addition, Fig. 16a and c demonstrate that the standard TP-1 test procedures for grain size measurement can lead to erroneous grain size data if the microstructure on the vertical section is not checked. The inclusion of such data in the theoretical analysis may exaggerate the solute effect on grain size [71,89].

Fig. 17 shows the calculated grain size data together with experimental data in Mg-Al alloys with and without intensive melt shearing under different solidification conditions, such as the standard TP-1 test ($\dot{T} = 3.5$ K/s) [69] and the high pressure die casting (HPDC) ($\dot{T} \approx 1000$ K/s) [91]. The dashed box in Fig. 17 highlights that the sample has a columnar grain structure which is not used to compare with the calculations. For Mg-Al melts, the nucleating particles are native

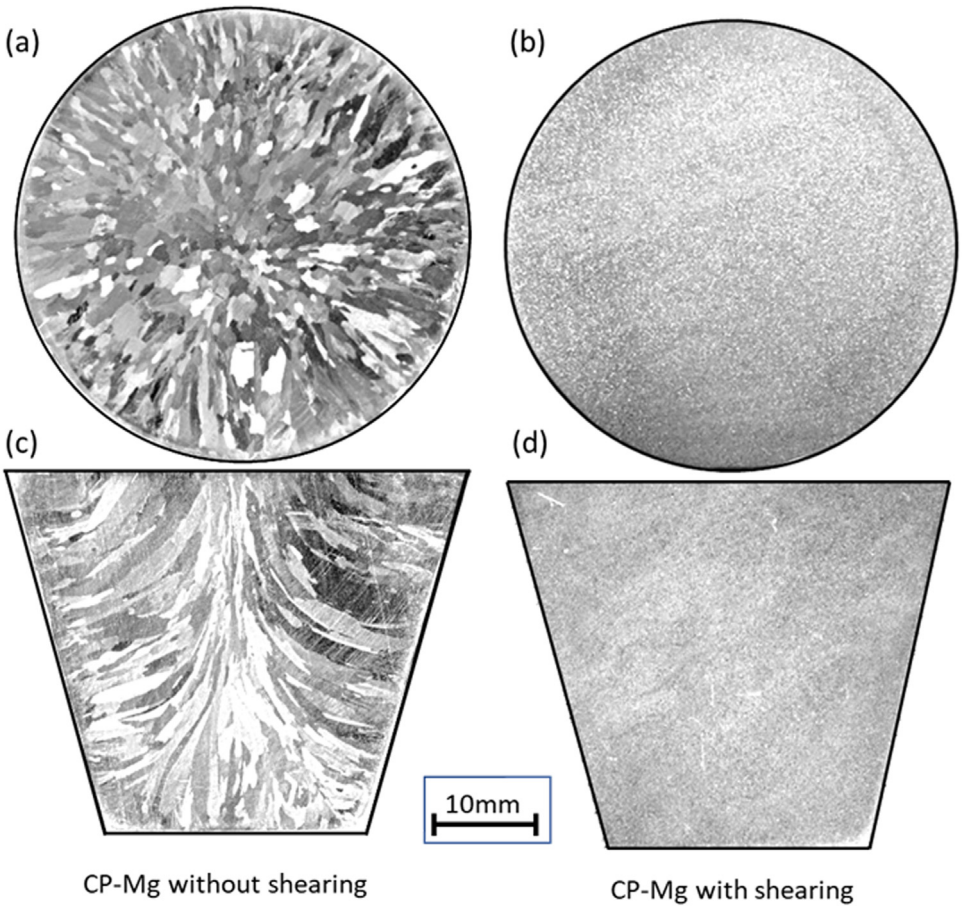

Fig. 16. Optical macrographs of CP-Mg solidified in a TP-1 mould. (a, c) Without intensive melt shearing; and (b, d) with intensive melt shearing. (a, b) are the cross sections and (c, d) are the vertical sections, showing the columnar structure of non-sheared CP-Mg and equiaxed structure of sheared CP-Mg.

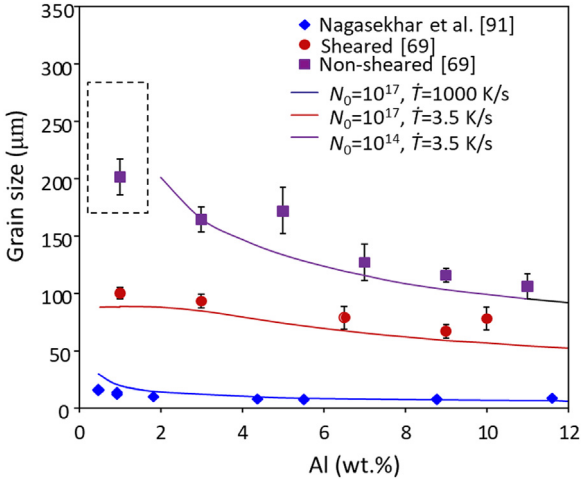

Fig. 17. The calculated grain size (solid lines) for Mg-Al alloys solidified under different conditions, showing a good agreement between calculations and experimental data [69,91].

MgO particles, which have a relatively large ΔT_n (1.2 K) due to their large lattice misfit with Mg [76] and atomically rough surfaces [59]. When Mg-Al alloys are solidified in the TP-1 mould without prior melt shearing, the N_0 of the MgO particles is approximately 10^{14} m^{-3} [82]. In this case, the grain initiation behaviour is PGI dominant, resulting in a relatively large grain size (the filled squares in Fig. 17). With prior melt shearing, the N_0 of the MgO particles increases to 10^{17} m^{-3} [82]. This increase in N_0 changes the grain initiation behaviour from PGI-dominant to EGI-dominant, resulting in a decrease in grain size (the filled circles in Fig. 17). In addition, HPDC allows the Mg-Al alloys to solidify at a high cooling rate (~10^3 K/s) and a high shear rate (~10^5 /s, comparable with intensive melt shearing) at the gate prior to solidification, leading to a more significant grain refinement (the filled diamonds [91] in Fig. 17).

These experimental results (Figs. 16 and 17) confirm that intensive melt shearing of Mg-alloys prior to casting leads to orders of magnitude increase in MgO particle number density which in turn results in a significant reduction of grain size. In addition, the results in Fig. 17 provide firm evidence to support that a high cooling rate promotes grain refinement, but solute concentration (growth restriction) has a limited effect on grain size.

In summary, the good agreement between experimental data and theoretical predictions over 3 orders of magnitude of grain size data provides strong validation of the current theoretical model for grain size prediction [69]. This comparison

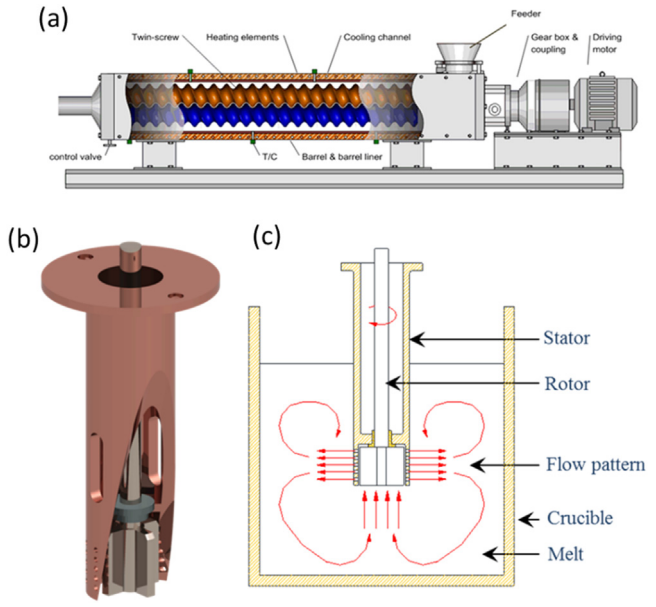

Fig. 18. Schematic illustration of the (a) twin-screw high shear unit [42,95], (b) rotor-stator high shear unit, and (c) macroscopic melt flow pattern around the tip of the rotor-stator high shear device [94,96].

in Fig. 17 also provides indirect validation of the concept of progressive and explosive grain initiation behaviour.

4. Applications to industrial casting processes

4.1. Dispersion of MgO particles by intensive melt shearing

To produce cast components/feedstock with fine and uniform solidification microstructure, we have developed a novel intensive melt shearing process to condition alloy melts prior to solidification processing [42,45,92–94]. The high shear process was initially embodied by a twin-screw machine [42,95] (Fig. 18a) and later by a simpler rotor-stator mechanism [94,96] (Fig. 18b). For the twin-screw high shear process (Fig. 18a), the liquid metal is fed into the device, in which a pair of co-rotating and fully intermeshing screws are rotating inside a heated barrel with accurate temperature control. The liquid metal in the twin-screw unit is subjected to intensive shearing under a high shear rate and high intensity of turbulence. Consequently, the conditioned liquid metal has extremely uniform temperature, uniform composition and well-dispersed inclusion particles [42]. The rotor-stator unit (Fig. 18b) comprises a rotor and a stator attached to an electrical motor with speed control. During its operation, the fast-rotating rotor inside the stator provides intensive shearing to the melt in the gap between the rotor and the stator and also in the openings on the stator. The rotation speed can be as high as 10,000 rpm providing a shear rate as high as 10^5 s^{-1}. This rotor-stator high shear device provides dispersive mixing action inside the rotor-stator device and distributive mixing outside the rotor-stator through the macro-flow patterns shown in Fig. 18c [94].

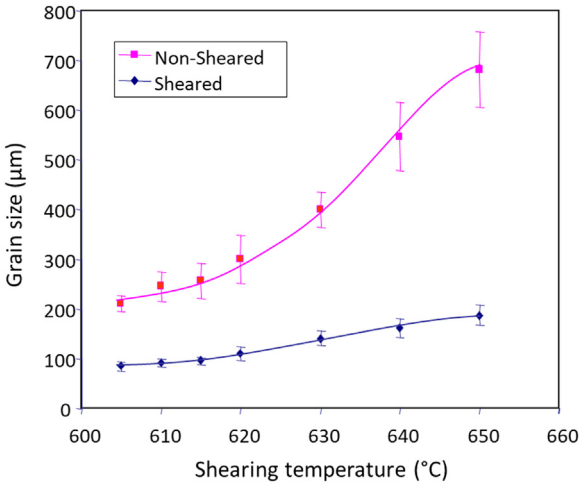

Fig. 19. Grain size of AZ91D alloy solidified in the TP-1 mould ($\dot{T}$ = 3.5 K/s) under different processing conditions showing the significant grain refinement by intensive melt shearing [43].

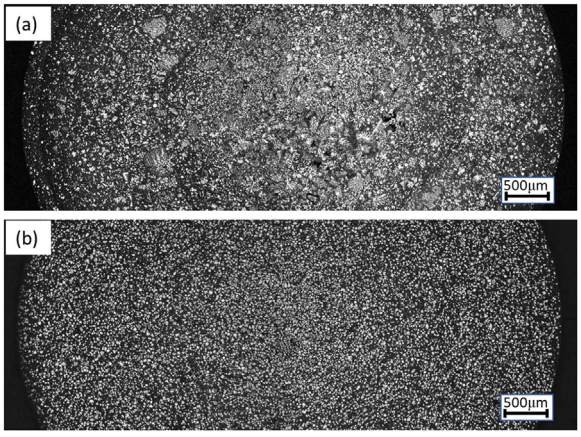

Fig. 20. Optical micrographs of AZ91D alloy produced by (a) the conventional HPDC process, and (b) the MC-HPDC process [100]. Intensive melt shearing leads to a fine and uniform microstructure with significantly reduced cast defects.

Here we show an example of the application of intensive melt shearing for grain refinement of Mg-alloys [43]. The AZ91D alloy melt was transferred to a preheated twin-screw unit and subjected to intensive shearing at different temperatures (605 to 650 °C) above the alloy liquidus with a rotation speed in the range of 500–800 rpm. The standard TP-1 test mould was used to cast AZ91 alloy with and without intensive melt shearing. The resultant grain size as a function of pouring temperature is presented in Fig. 19 [43]. Without melt shearing, the grain size increases significantly with the increase in pouring temperature, while with intensive melt shearing the grain size is much finer at all the pouring temperatures. In addition, melt shearing not only provides significant grain refinement but also reduces grain size dependence on the pouring temperature [43]. Further investigations [82] show that intensive melt shearing can effectively disperse the usual oxide films and oxide skins into more discrete particles, resulting in a significant increase in MgO particle number den-

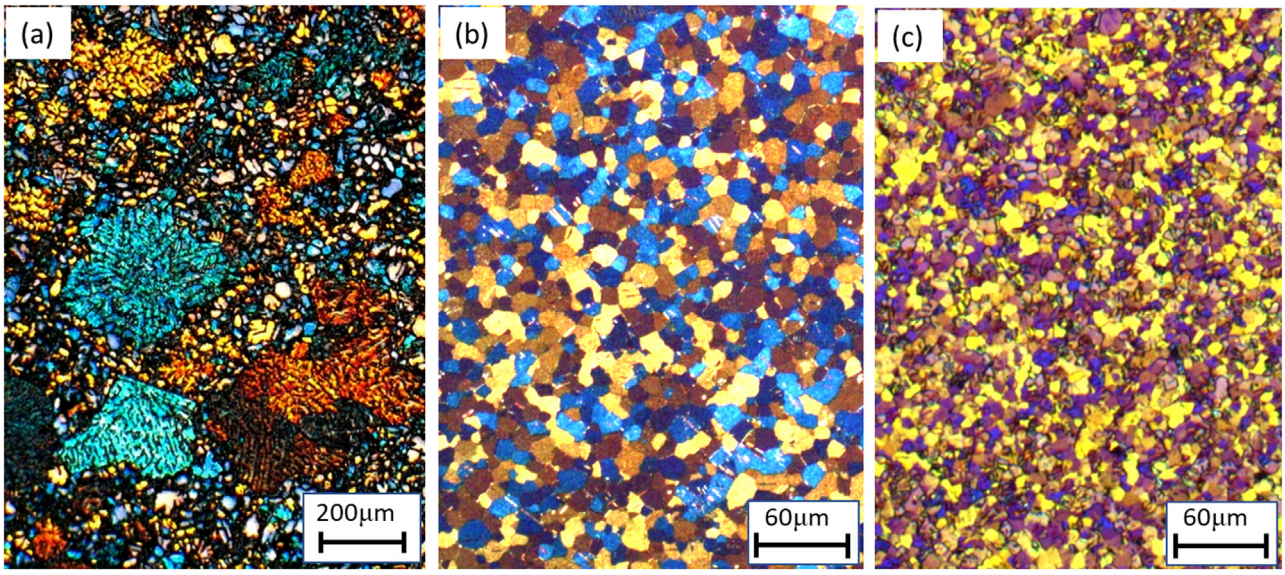

Fig. 21. Optical micrographs showing the microstructures of Mg-alloys produced by the HPDC process [68]. (a) Mg-9Al-1Zn without intensive melt shearing, the average grain size is 200 μm; (b) Mg-1Zr-1Ca alloy with intensive melt shearing, the average grain size is 20 μm; and (a) CP-Mg with intensive melt shearing, the average grain size is 6 μm.

sity from 10^{14} m^{-3} without shearing to 10^{17} m^{-3} with shearing. It was confirmed that such dispersed MgO particles do act as heterogeneous nucleation sites for effective grain refinement [43].

4.2. Melt conditioning-high pressure die casting (MC-HPDC) process

HPDC has been the workhorse of the automotive industry due to its unique characteristics, such as low-cost, high efficiency and high volume for component production [97]. However, the HPDC process suffers from a number of drawbacks, such as high volume fraction of porosity, non-uniform microstructure, the existence of defect band and particularly inconsistency of mechanical performance of cast components. Intensive melt shearing prior to HPDC seems to offer a unique solution to such problems [42,98–107]. Fig. 20 compares the microstructures of AZ91D alloy bars with a 6 mm diameter produced by the conventional HPDC (Fig. 20a) and by the MC-HPDC process (Fig. 20b) [100]. Intensive melt shearing disperses the usual oxide films into more discrete MgO particles resulting in a 3-order magnitude of increase in MgO particle number density [82]. The combination of the high number density of nucleant particles and high cooling rate leads to a significant increase in the total number of grain initiation events, and thus a fine and uniform solidification microstructure throughout the entire components (Fig. 20b). This in turn reduces/eliminates the condition for the formation of cast defects, providing a component with high integrity and improved mechanical performance [100]. Grain refinement of HPDC Mg-alloys by intensive melt shearing is further demonstrated in Fig. 21 [68]. The conventional HPDC process produces AZ91D alloy samples with a 200 μm grain size (Fig. 21a); with intensive melt shearing the grain size of Mg-1Zr-1Ca alloy is reduced to 20 μm (Fig. 21b), and 6 μm for CP-Mg (Fig. 21c) [68].

4.3. Melt conditioning-direct chill (MC-DC) casting process

Direct-chill (DC) casting produces [108] Mg-alloy billets or slabs as feedstock for subsequent thermomechanical processing, such as extrusion and rolling. A grain-refined as-cast microstructure is desirable for two major reasons [108]: (1) a fine and equiaxed solidification process leads to a reduction in both macro-segregation and cast defects, which will, in turn, facilitate the subsequent thermomechanical processing; and (2) grain refinement and its consequences result in improved mechanical performance, particularly those properties closely related to local stress concentration, such as ductility, fatigue strength and fracture toughness. However, currently, there are no effective grain refiners available to deliver grain refinement of Mg-alloys. In recent years, the implementation of intensive melt shearing in the DC sump has led to the development of a novel MC-DC process [109–119] (Fig. 22a). The MC-DC process provides for the first time an effective approach for *in situ* control of microstructures during DC casting process. Fig. 22b is an optical micrograph showing the sharp microstructural transition from a coarse equiaxed dendritic structure with a millimetre level of grain size to fine and equiaxed dendrites by switching on the rotor/stator high shear device during DC casting of AZ91D alloy [111].

Intensive melt shearing in the DC sump disperses the usual oxide films into more discrete MgO particles and leads to a 3-order magnitude increase in MgO number density, which in turn results in a significant grain refinement according to the grain refinement maps (Fig. 15). In addition, intensive melt shearing ensures a controlled and uniform sump temperature and a uniform chemical composition, creating a favourable

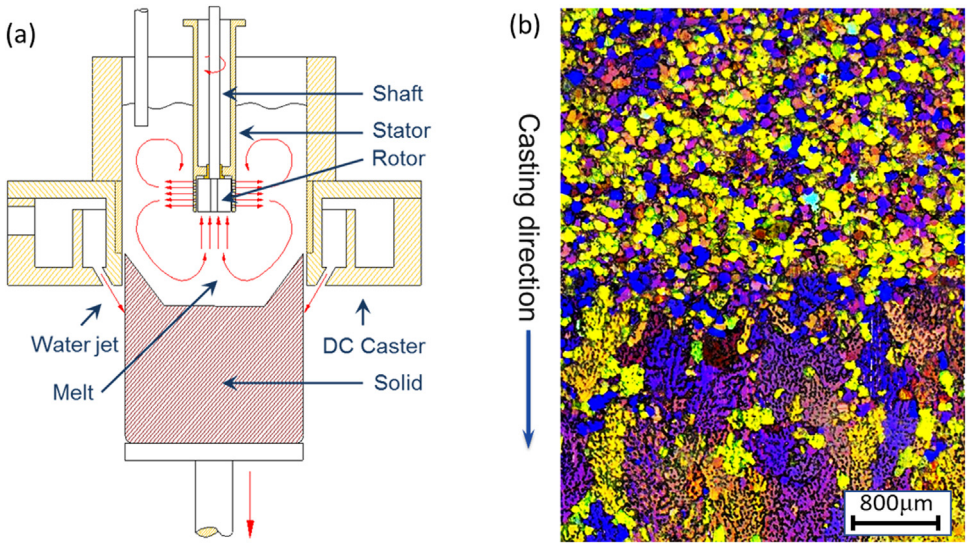

Fig. 22. (a) Schematic illustration of the MC-DC casting process where an intensive melt shearing device is submerged in the sump of the DC caster; (b) optical micrograph showing the immediate microstructural transition of DC cast AZ91D alloy from a coarse grain structure (bottom half of (b)) to a refined grain structure (top half of (b)) when the rotor-stator high shear device is switched on [111].

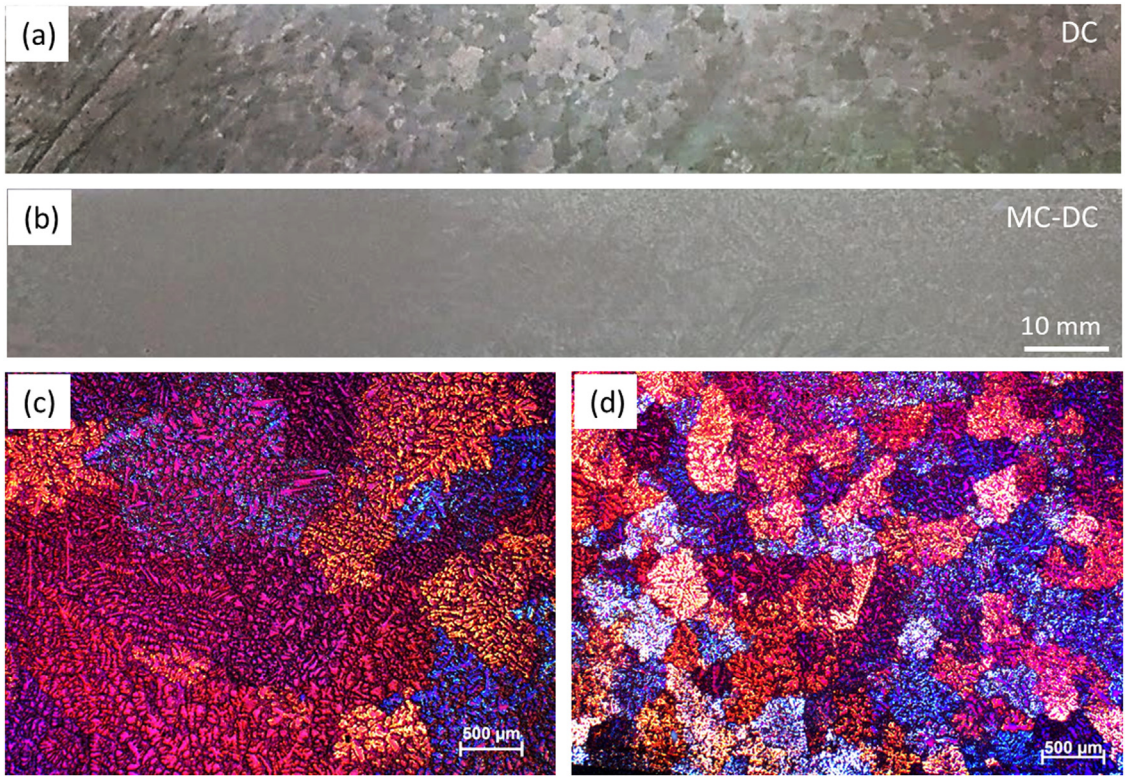

Fig. 23. Optical micrographs of cast AZ80 alloy billet (300 mm diameter) by (a, c) the conventional DC casting process and (b, d) the MC-DC casting process.

and consistent solidification condition. The overall effect of intensive melt shearing is a fine and uniform microstructure throughout the entire DC billet with significantly reduced or eliminated macro-segregation, porosity and surface defects, as demonstrated in Fig. 23 by the grain structures of MC-DC cast AZ80 alloy billet (300 mm diameter) in comparison with that produced by the conventional DC casting process.

Intensive melt shearing in the DC sump provides also an effective means for accurate sump temperature control. With an appropriately selected rotation speed, the sump temperature is not only uniform but can be accurately controlled to be a few degrees above the alloy liquidus. This leads to a significantly reduced distance between the liquidus and solidus isotherms. Under a constant casting speed, this means a pro-

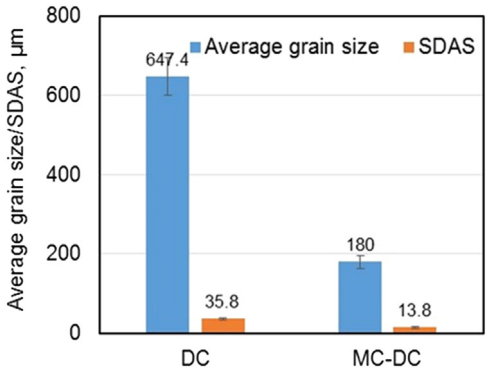

Fig. 24. Intensive melt shearing in the DC sump (MC-DC) leads to simultaneous refinement of grain size and secondary dendritic arm spacing (SDAS) of AZ31 alloy billet in comparison with the same alloy produced by conventional DC casting.

portional reduction of solidification time (the time a solid particle stayed between the liquidus and solidus isotherms). According to the dendrite growth theory [120], the ultimate effect of intensive melt shearing is a significant reduction of secondary dendrite arm spacing (SDAS), as shown in Fig. 24. A refined SDAS causes the last-to-solidify liquid (usually multi-component eutectic) to be finely dispersed in the inter-dendrite arm regions, leading to refined and uniformly distributed second phase particles, as demonstrated in Fig. 25 by the refined and uniformly distributed β-$Al_{17}Mg_{12}$ phase in the MC-DC cast AZ31 billet.

4.4. Melt conditioned twin-roll casting (MC-TRC) process

Twin roll casting (TRC) combines casting and hot rolling into a single step for producing strips close to their final thickness, reducing the need for hot or cold rolling, which is particularly attractive for Mg-alloys [121–123]. However, the conventional TRC process emphasises the importance of the deformation part of the process taking little advantage of the casting process. This causes the solute-rich liquid to segregate to the centre of the strip leading to a severe centre-line segregation and surface bleed, which decreases the ductility of the as-cast strip, extends the homogenisation time and increases the production cost. Thus, currently, only very dilute alloys may be efficiently processed with the conventional TRC. The grand challenges in TRC research include: (1) reducing/eliminating centre-line segregation; (2) reducing/eliminating the strong basal texture in the as-cast strip; and (3) increasing cast speed thus increasing productivity.

In the LiME Hub, we have developed a novel MC-TRC process [124–135]. The MC-TRC process (Fig. 26 [131]) has the following advantageous features:

- Intensive melt shearing prior to TRC disperses the usual oxide films into discrete MgO particles, increasing MgO number density from 10^{14} to 10^{17} m^{-3} [82]. The high particle number density of MgO, with low nucleation potency, high particle number density and high cooling rate ensure a high density of grain initiation events during TRC and thus a fine and equiaxed solidification process (Fig. 27 [130]). Consequently, MC-TRC eliminates the coarse columnar grain structures and thus significantly reduces or even eliminates the possibilities of centre-line segregation and surface bleed (Fig. 28 [45]).

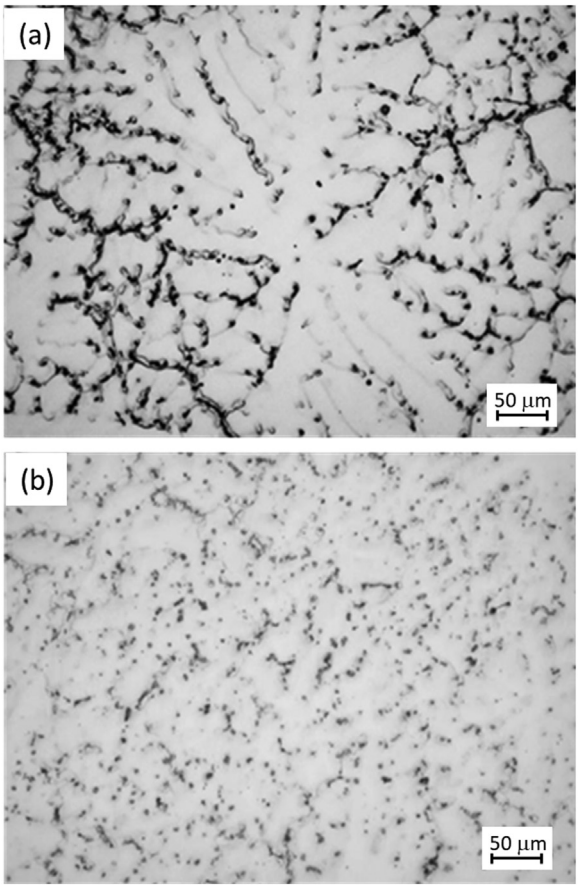

Fig. 25. Micrographs of DC cast AZ31 alloy showing that intensive melt shearing leads to refined and well-dispersed second phase particles (β-$Al_{17}Mg_{12}$ in this case). (a) Without intensive melt shearing; and (b) with intensive melt shearing.

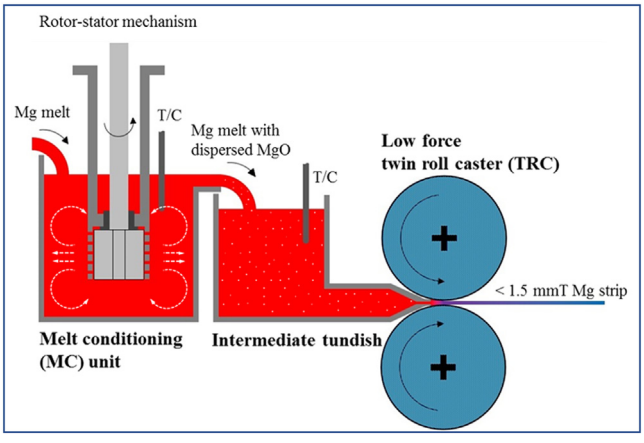

Fig. 26. Schematic illustration of the MC-TRC process [131]. Melt-conditioning unit [96] provided intensively sheared alloy melt to a low force twin roll caster via an intermediate tundish.

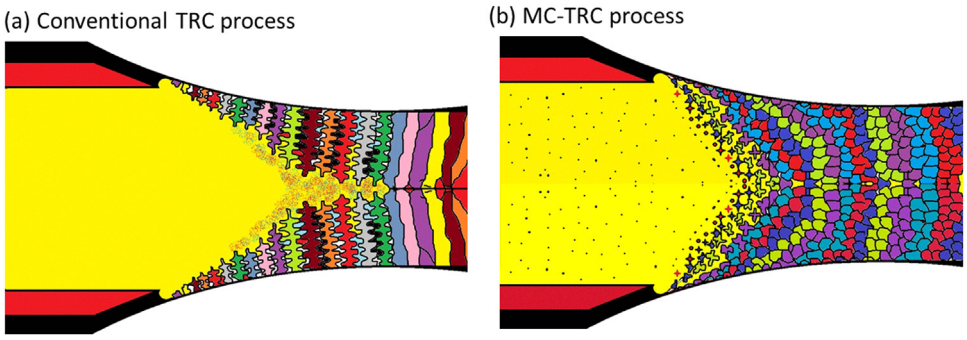

Fig. 27. Schematic illustration of the solidification process in (a) the conventional TRC process and (b) the MC-TRC process [130].

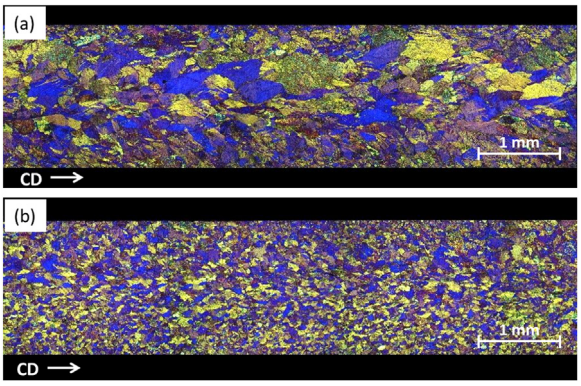

Fig. 28. Microstructures of as-cast AZ31 strips produced by (a) TRC and (b) MC-TRC, showing significant grain refinement and improved microstructural uniformity [45].

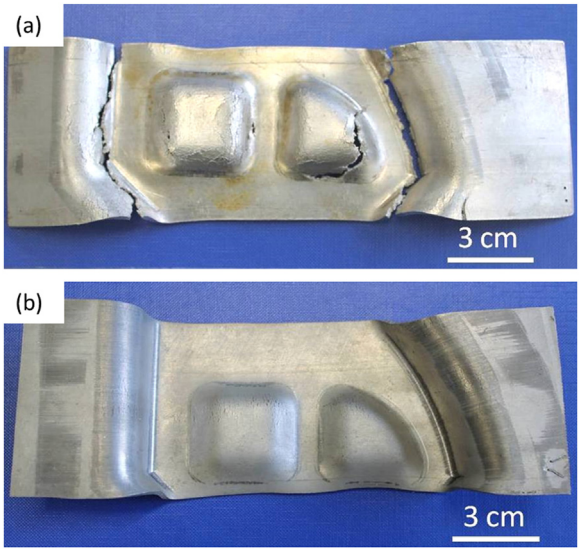

Fig. 30. Pictures of AZ31 alloy strip after hot stamping at 450 °C [128]. (a) Conventional TRC strip; and (b) MC-TRC strip. After stamping, the TRC strips show severe cracking while the MC-TRC strips are crack free.

- A small roll diameter provides a large opening for the tundish tip to move closer to the roll nip resulting in a smaller deformation zone and a reduction of strip thickness, being as thin as 1 mm. The overall effect is an increased cast speed and reduced production cost.
- The emphasis on the importance of casting in the MC-TRC process makes it possible to reduce substantially the rolling force, changing the TRC microstructure from a largely deformed structure with strong basal texture (Fig. 28a) to a solidification structure with more random grain orientations (Fig. 28b) [45]. The grain size reduction by intensive melt shearing can be as much as an order of magnitude.
- MC-TRC ensures a fine, uniform and almost defect-free microstructure through the entire strip thickness, which in

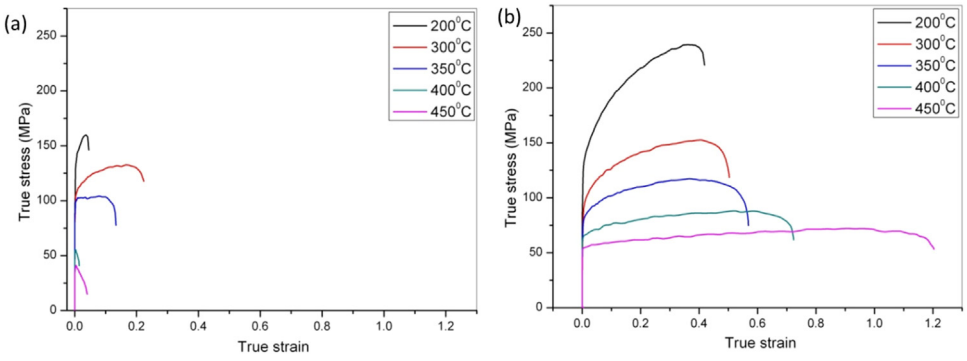

Fig. 29. True stress-strain curves for as-cast AZ31 strip tested at different temperatures [128]. (a) Conventional TRC strip; and (b) MC-TRC strip. The strips produced by traditional TRC have low strength, low ductility and irregular temperature dependence, suggesting that the TRC strips have severely defected. On the opposite, the MC-TRC strips have significantly improved strength and ductility predictable temperature dependence, suggesting that the MC-TRC strips are free from critical defects.

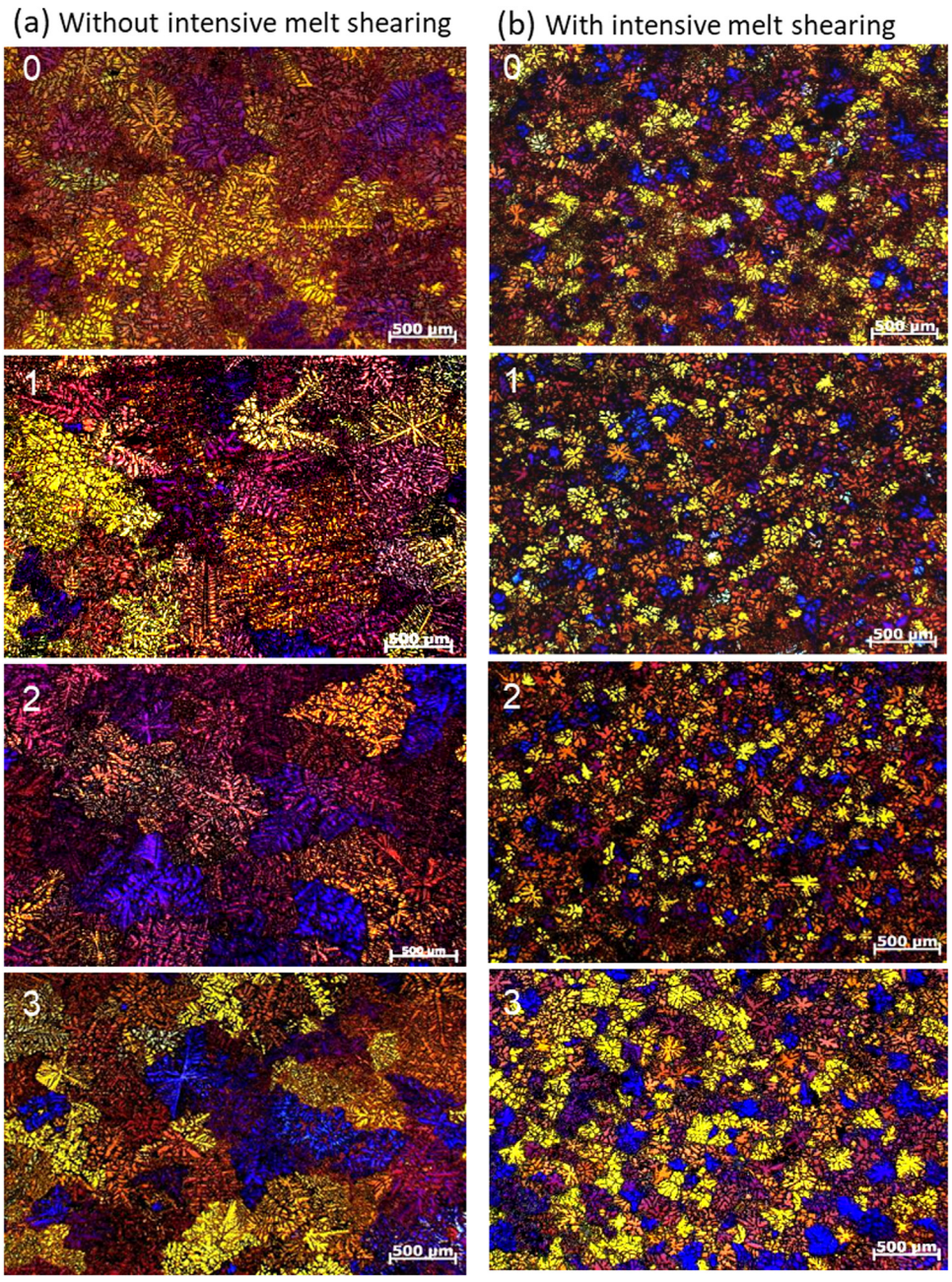

Fig. 31. Optical micrographs showing the grain structures of AZ91D alloy repeatedly re-melted and re-solidified in a TP-1 mould ($\dot{T} = 3.5$ K/s). (a) Without the initial melt shearing; and (b) with the initial melt shearing. The numbers in the micrographs indicate the number of times of re-melting.

turn leads to a high and consistent mechanical performance (Fig. 29) [128].

- It has been successfully demonstrated that the MC-TRC strip can be directly hot-stamped without any need for prior rolling (Fig. 30) [128]. This provides a commercial opportunity for the production of 3C packaging by direct stamping of the MC-TRC Mg thin strips.

4.5. Self-grain-refining Mg-alloy ingot

Our research has confirmed that the grain refining effect of intensive melt shearing can be sustained even after repeated remelting and casting without the need for further intensive melt shearing [136]. The intensively sheared AZ91 alloy melt was cast into the TP-1 mould, and the produced TP-1 ingot was then remelted and recast repeatedly without further intensive melt shearing. The reference samples were produced by repeatedly melting and casting AZ91D alloy without any intensive melt shearing. The resultant microstructures are compared in Fig. 31. Intensive melt shearing of AZ91D alloy melt results in well-dispersed MgO particles, a high MgO particle density in the alloy melt and ultimately a fine grain size (below 200 μm) in the as-cast TP-1 ingot. Repeatedly remelting and casting may cause two opposite effects: (1) increased

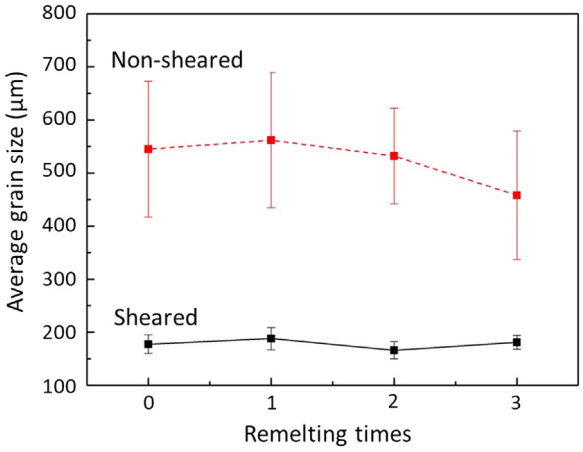

Fig. 32. Grain size of AZ91D alloy repeatedly re-melted and re-solidified in a TP-1 mould ($\dot{T}$ = 3.5 K/s) as a function of the number of times of re-melting.

MgO number density due to further oxidation during melt handling and casting; and (2) decreased MgO number density due to re-agglomeration of the initially dispersed MgO particles in the melts and during solidification. The experimental results in Fig. 31 suggest that the MgO particle number density in the repeatedly remelted samples is sufficiently high to sustain the level of grain refinement without the need for further intensive melt shearing. However, this is not the case for the reference samples (without the initial intensive melt shearing), where the grain size of the repeatedly remelted and recast samples is constantly larger than 500 μm (Fig. 32).

The results from repeatedly remelting and recasting suggest that Mg-alloys can be made self-grain refining if the alloy ingots were cast with prior intensive melt shearing. The self-grain refining ingot has a fine and uniform microstructure across the entire ingot (Fig. 33) [136,137].

4.6. High shear recycling

The recycled Mg-alloys contain an increased amount of oxide skins, oxide films, impurity elements and other inclusions, which makes direct in-house recycling of Mg-scrap impossible. Mg-alloy scraps are usually collected and recycled in a dedicated recycling centre with a complex melt treatment process [138]. However, the dispersing power of intensive melt shearing may be used not only to eliminate the harmful effect of oxide films and other inclusions but also to make them available for grain refinement without the addition of grain refiners. This is demonstrated in Fig. 34 by the mechanical performance of AZ91D alloys produced by HPDC from feedstock with different contents of directly recycled scraps [138]. It is not surprising to note that both the strength and ductility of HPDC AZ91D from 100% diecast scrap match well those from 100% primary alloys. This is a very encouraging result since it means that diecasting foundries can recycle their scrap in-house without compromising the mechanical performance of their HPDC components as long as they fully shear their melts with scrap addition. It is also clear that this direct recycling approach is applicable to all casting processes, including continuous casting as long as the Mg melts with recycled contents are fully treated by the high shear process. Obviously, further research is required to understand corrosion resistance and other chemical and physical properties of the Mg-alloys with directly recycled contents.

5. General discussions

5.1. The addition of more potent particles than MgO will not lead to more grain refinement

The traditional wisdom for grain refinement is to promote heterogeneous nucleation (reducing ΔT_n) by adding grain refiners that contain potent nucleant particles of significant number density [46–52,80]. This approach is clearly demonstrated by the two well-known commercial grain refiners, Al-Ti-B-based grain refiners for Al-alloys [80,139] and Mg-Zr-based grain refiners for Mg-alloys [48,140]. In the case of Al-Ti-B-based grain refiners, TiB_2 particles have a lattice misfit of -4.22% with Al and are therefore relatively impotent for nucleating Al. However, a (1 1 2)Al_3Ti 2DC forms on (0 0 0 1) TiB_2 surface during the grain refiner production process and reduces the absolute value of the misfit from the original 4.22% to 0.09%, rendering the TiB_2/Al_3Ti 2DC particles extremely potent for nucleating Al [80]. In addition, from a nucleation competition point of view, such potent particles ensure that there is no other solid particle of significance for heterogeneous nucleation. Similarly, in the case of Mg-Zr-based grain refiners for Mg-alloys, the same crystal structure and closely matching crystal lattice parameters between Zr and Mg make Zr a very potent substrate for the heterogeneous nucleation of Mg [78]. It should be pointed out that such success in grain refinement relies on the specific chemical and physical characteristics of the liquid/substrate interface at the moment of heterogeneous nucleation. Any changes in the interfacial characteristics prior to heterogeneous nucleation may alter the pathway of heterogeneous nucleation and grain initiation, resulting in a different outcome for grain refinement. For instance, the existence of 500 ppm Zr in Al-alloys makes TiB_2-based grain refiners ineffective for grain refinement [141], and Mg-Zr-based grain refiners do not work for Al-containing Mg-alloys [48], all due to chemical reactions at the substrate/liquid interface prior to heterogeneous nucleation.

Here we demonstrate that this traditional approach for grain refiner development is not effective for Mg-alloys, i.e., the addition of more potent particles than native MgO will not lead to more effective grain refinement of Mg-alloys than the native MgO particles do. Just imagine that there is a group of hypothetical solid particles that have the same particle size distribution as MgO particles (d_0 = 0.07 μm and σ = 0.45) but have different nucleation undercooling (ΔT_n). Fig. 35 shows the calculated grain size as a function of nucleation undercooling and two different particle number densities (N_0 = 10^{14} and 10^{17} m^{-3}) for Mg-1Al alloy solidified at a cooling rate of 3.5 K/s. The dotted line represents

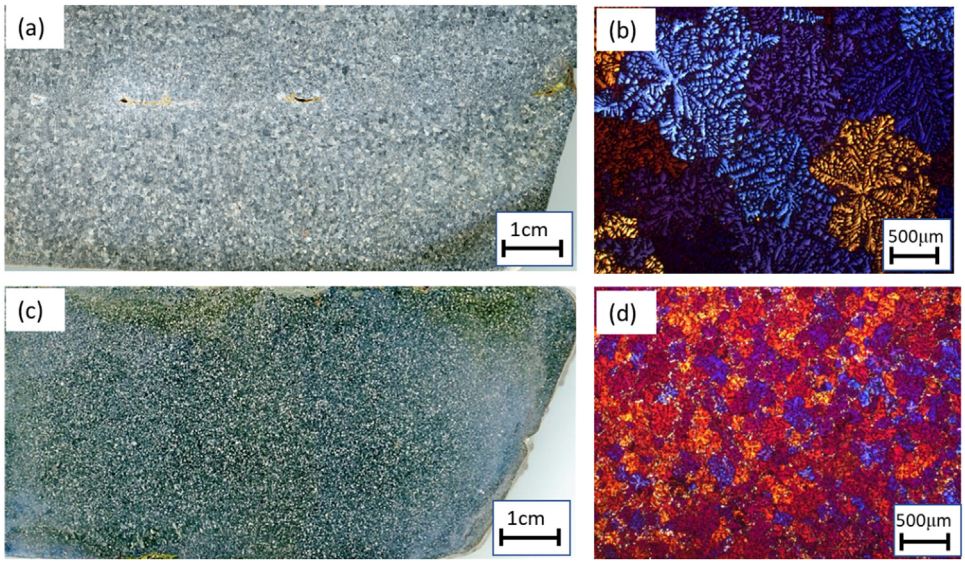

Fig. 33. Optical graphs of AZ31 melt-conditioned cast ingot showing a fine and uniform grain structure upon final solidification after application of intensive melt shearing [136,137]. (a, c) Macrostructure and (b, d) microstructure; and (a, b) without and (c, d) with intensive melt shearing.

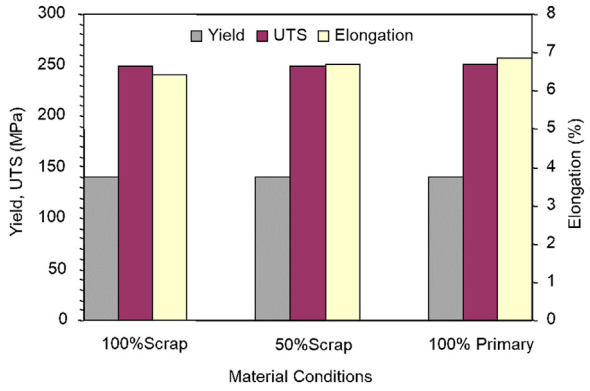

Fig. 34. Performance of high shear recycled AZ91D alloy produced by MC-HPDC [138].

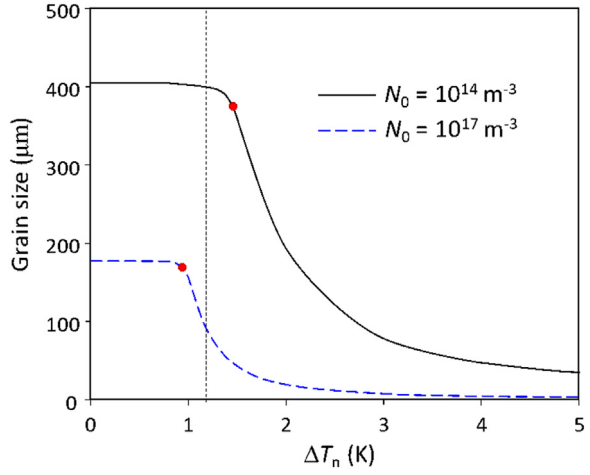

Fig. 35. Calculated grain size of Mg-1Al alloy solidified at $\dot{T} = 3.5$ K/s and inoculated by hypothetical solid particles with varying nucleation undercooling (ΔT_n) at two different particle number densities (N_0) but with the same log-normal size distribution ($d_0 = 0.07$ μm, $\sigma = 0.45$). The red dots mark the position where PGI and EGI have equal numbers (N_{EGI}:$N_{PGI} = 1$), and the dotted line represents MgO particles with estimated $\Delta T_n = 1.2$ K.

$\Delta T_n = 1.2$ K, which is the estimated ΔT_n for MgO, and the red dots mark the positions where the numbers of PGI and EGI events are equal, which delineate the PGI dominant zone from the EGI dominant zone. When $N_0 = 10^{14}$ m^{-3}, grain initiation is PGI-dominant; when the addition of more potent particles (decreasing ΔT_n) with the same N_0 and size distribution as MgO particles is made, the grain size does not decrease but increases slightly. This suggests that the addition of more potent particles will not lead to more grain refinement. When the N_0 increases to 10^{17} m^{-3}, grain initiation changes to EGI-dominant and the grain size is significantly reduced. Similarly, the addition of more potency particles with the same N_0 and size distribution as MgO particles increases substantially the grain size. However, in both cases, the addition of more impotent particles (increasing ΔT_n) will result in more significant grain refinement for both $N_0 = 10^{14}$ and 10^{17} m^{-3} if native MgO particles can be completely removed from the melt. This will be discussed further later.

It can be concluded from this analysis that the addition of more potent nucleant particles than MgO will not lead to more grain refinement than native MgO particles do. This suggests that the current search for effective grain refiners for Mg-alloys (particularly Mg-Al alloys) by addition of more potent particles than MgO will need to change direction, from searching for more potent particles to enhance heterogeneous nucleation to searching for more impotent particles to impede heterogeneous nucleation: (1) making native MgO particles themselves more impotent; and (2) adding more impotent particles but removing completely the native MgO particles.

5.2. Making native MgO more potent will not lead to more grain refinement

The solute segregated at the liquid/substrate interface may form 2DC or 2DS (2 dimensional-solution) to change the nucleation potency of the substrate due to the changes in lat-

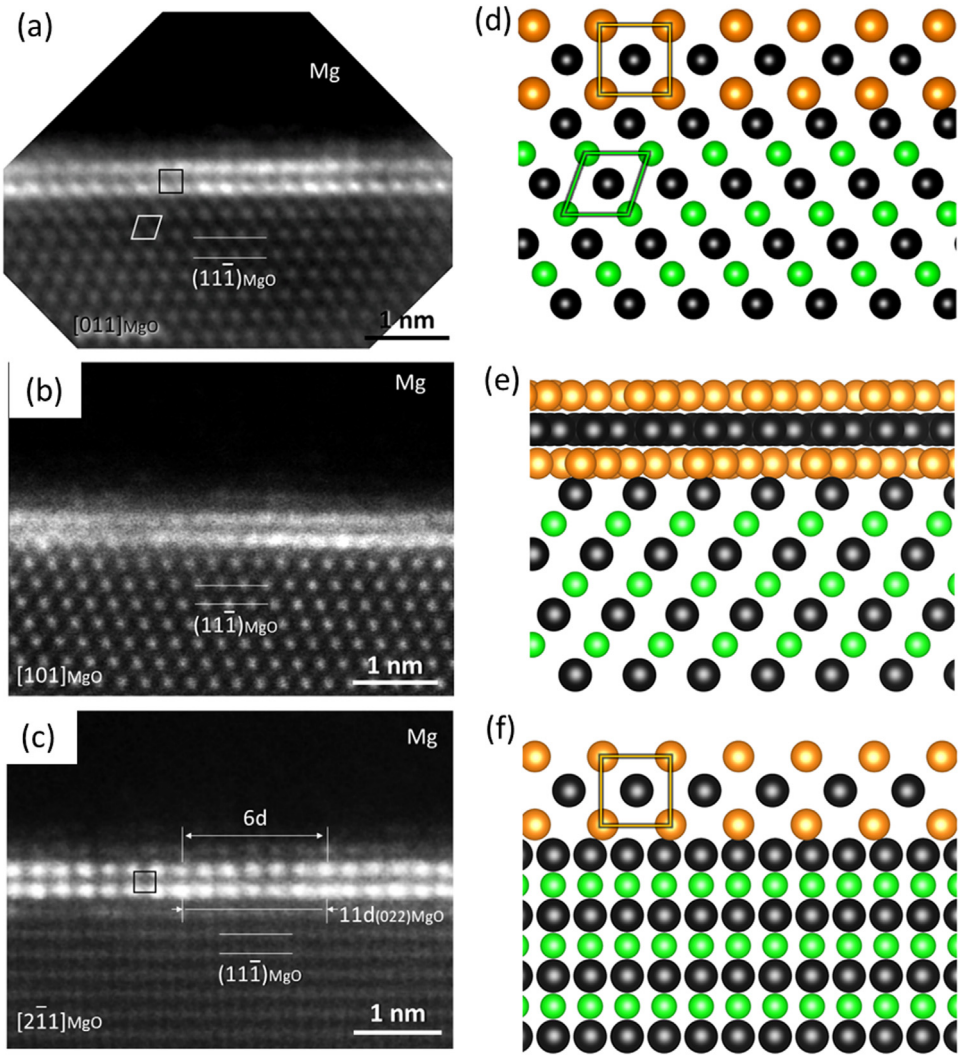

Fig. 36. High resolution HAADF STEM images of the Mg/MgO (1 1 1) interface in Mg-0.5Y alloy [142] observed along (a) [0 1 1], (b) [1 0 1] and (c) [2 $\bar{1}$ 1] directions, showing two atomic layers with a brighter contrast, which are identified as Y_2O_3 2DC. Schematics showing the atomic configuration of Y (orange) and O (black) in the Y_2O_3 2DC at Mg/MgO{1 1 1} interface (Mg atoms are shown in green) viewed along (d) $[0\ 1\ 1]_{MgO}$, (e) $[1\ 0\ 1]_{MgO}$ and (f) $[2\ \bar{1}\ 1]_{MgO}$ directions.

tice misfit, surface roughness or chemical potential. In Mg-Y alloys, Wang [142,143] found that O and Y co-segregate on the MgO {1 1 1} facet and form a Y_2O_3 2DC layer, as shown in Fig. 36. According to the high angle annular dark-field (HAADF) scanning transmission electron microscopy (STEM) images from different directions, the OR between {1 1 1}MgO and {1 0 0}Y_2O_3 2DC was established as:

$$\left(1\,1\,\bar{1}\right)\left[2\,\bar{1}\,1\right]\mathrm{MgO}//(1\,0\,0)\,[0\,0\,1]\ Y_2O_3-2\mathrm{DC}. \quad (6)$$

As a result, the Y_2O_3-2DC replaces MgO as the new substrate templating the nucleation of Mg grain. The most likely OR as Wang [142] suggested is

$$\{1\,0\,0\}\langle 1\,0\,0\rangle\ Y_2O_3-2\mathrm{DC}//\{0\,0\,0\,1\}\langle 1\,0\,\bar{1}\,0\rangle\mathrm{Mg}. \quad (7)$$

The formation of {1 0 0}Y_2O_3 2DC on MgO{1 1 1} changes the lattice misfit from the original 7.9% between MgO and Mg to 1.7% between {1 0 0}Y_2O_3 2DC and Mg. Moreover, the surface layer of {1 0 0} Y_2O_3 2DC contains Y atoms only, which are strongly attracted to the Mg atoms in liquid due to the negative mixing enthalpy between Y and Mg, and thus enhance the nucleation potency of {1 0 0}Y_2O_3 2DC [58,142]. Both the reduced misfit and increased chemical interaction make the MgO{1 1 1} particles coated with Y_2O_3 2DC more potent than the original MgO{1 1 1) with a clean surface. However, the experimental results from the TP-1 test have confirmed that the grain size of Mg-0.1Y alloy with intensive melt shearing is 105 μm, comparable with 100 μm for Mg-1Al alloy with intensive melt shearing. This has confirmed that making MgO particles more potent will not lead to more effective grain refinement, being consistent with the conclusions from the previous section.

5.3. It is difficult to make native MgO more impotent for more effective grain refinement

As suggested in Fig. 35 and discussed in Section 5.1, more significant grain refinement can be achieved by the addition of more impotent particles than MgO to impede heteroge-

neous nucleation. Perhaps the most convenient way to do so is to make the native MgO particles more impotent by chemical segregation at the interface between liquid Mg and MgO substrate, by either increasing the lattice misfit [56,63–65] or increasing the substrate surface roughness at the atomic level [57] or enhancing the repulsive interaction between the liquid and substrate atoms [58]. However, this might be a mission impossible, since the lattice misfit is already high (7.9%) [76] and the surfaces of both MgO{1 1 1} and MgO{1 0 0} are already rough [59]. This is further demonstrated by the following two cases.

In Mg-Ca alloy, Wang [142,144] observed an adsorption layer with a thickness of around 1 nm at the Mg/MgO interface, which has the same structure as the adjacent MgO. HAADF imaging and electron energy loss spectroscopy (EELS) analysis were used to characterize both the Mg/MgO {1 1 1} and Mg/MgO {1 0 0} interfaces. The results showed that the segregation layers had the same structure as MgO; both Mg and O were deficient in the segregation layer, whilst the Ca and N were concentrated, indicating that Mg and O atoms on the MgO surface were substituted by Ca and N atoms, respectively. Such a substitutional process will lead to the formation of vacancies and local atomic re-configuration, resulting in an atomically rough surface. Albeit the lattice misfit is not changed, the atomically rough surface will reduce the nucleation potency [57], which in turn impedes the heterogeneous nucleation. The experiments [142,144] confirmed that the grain size of Mg-Ca alloy (0.3-1.0 Ca) with intensive melt shearing is between 95 and 162 μm, being comparable with that of CP-Mg with intensive melt shearing. The slight decrease in grain size with increasing Ca addition may be attributed to the increased dispersion of MgO particles due to reduced interfacial energy rather than a change in the potency of MgO particles.

Sn is also experimentally confirmed to segregate onto the surface of MgO in Mg-Sn alloys. Similar to the case of Mg-Ca alloys, segregation of Sn at the Mg/MgO interface does not alter the lattice misfit but introduces vacancies and atomic displacement in the segregated layer, leading to an increase in surface roughness at the atomic level that impedes heterogeneous nucleation [142]. The grain size of Mg-Sn alloys is only moderately reduced compared to CP-Mg, and this slight reduction in grain size is most likely caused by the dispersion of MgO particles due to reduced interfacial energy rather than by decreased nucleation potency.

5.4. There is little space for developing successful grain refiners for Mg-alloys

The benchmarking position for developing new grain refiners is native MgO. The new grain refiners have to be more effective for grain size reduction than the native MgO particles themselves. Based on the concept of grain refinement maps presented in Section 3.4, successful grain refiners can be developed through the following potential approaches:

(1) Reducing nucleation undercooling (ΔT_n) to enhance heterogeneous nucleation. This will promote PGI for grain refinement.
(2) Increasing nucleation undercooling by making native MgO particles more impotent. This will promote EGI for grain refinement.
(3) Reducing the mean size and narrowing the size distribution (close to mono-size) of the operating particles (particles that initiate grains). This will increase the number of grain initiation events before recalescence for grain refinement.

Based on our previous discussions, particles that promote explosive grain initiation will result in finer grain size. Approach (1) promotes progressive grain initiation and will not be more effective for grain refinement than the native MgO particles. This approach has been utilised to develop new grain refiners, particularly for Mg-Al alloys, and has had little commercial success [48,52]. Approach (2) involves making native MgO particles more impotent, which is very difficult to achieve since MgO particles having a large lattice misfit with Mg and an atomically rough surface are already very impotent. Approach (3) is not practical since the native MgO particles are not only fine in mean particle size but also difficult to change their natural size distribution (log-normal). Therefore, we can conclude that there is little space for the development of new grain refiners that can be more effective than native MgO particles.

5.5. Grain refining Mg-alloys by intensive melt shearing

As we have discussed previously, there is little space to develop effective grain refiners for Mg-alloys by using either more potent particles to promote progressive grain initiation or more impotent particles to promote explosive grain initiation. Instead of chemical inoculation (addition of grain refiners), perhaps the most straightforward way to grain refine Mg-alloys is the physical dispersion of native oxide.

Native MgO in Mg-alloys has a large lattice misfit with Mg (7.9%), an atomically rough surface due to surface vacancies and vertical displacement of the surface Mg atoms and a large particle number density (10^{17} m^{-3}). According to the grain refinement maps presented in Figs.14 and 15, all these characteristics put native MgO in a good position for effective grain refinement of Mg-alloy. The only action required for achieving effective grain refinement is to disperse the native MgO particles to make the best use of all the available MgO particles. This proposition has been supported by our recent experimental results.

- We found out that the application of intensive melt shearing in the DC casting process (i.e., the MC-DC process) can result in grain refinement in all the Mg-alloys we have tried so far, and this grain refinement is independent of alloy compositions. As shown in Fig. 37, all the MC-DC Mg-alloys have a grain size of around

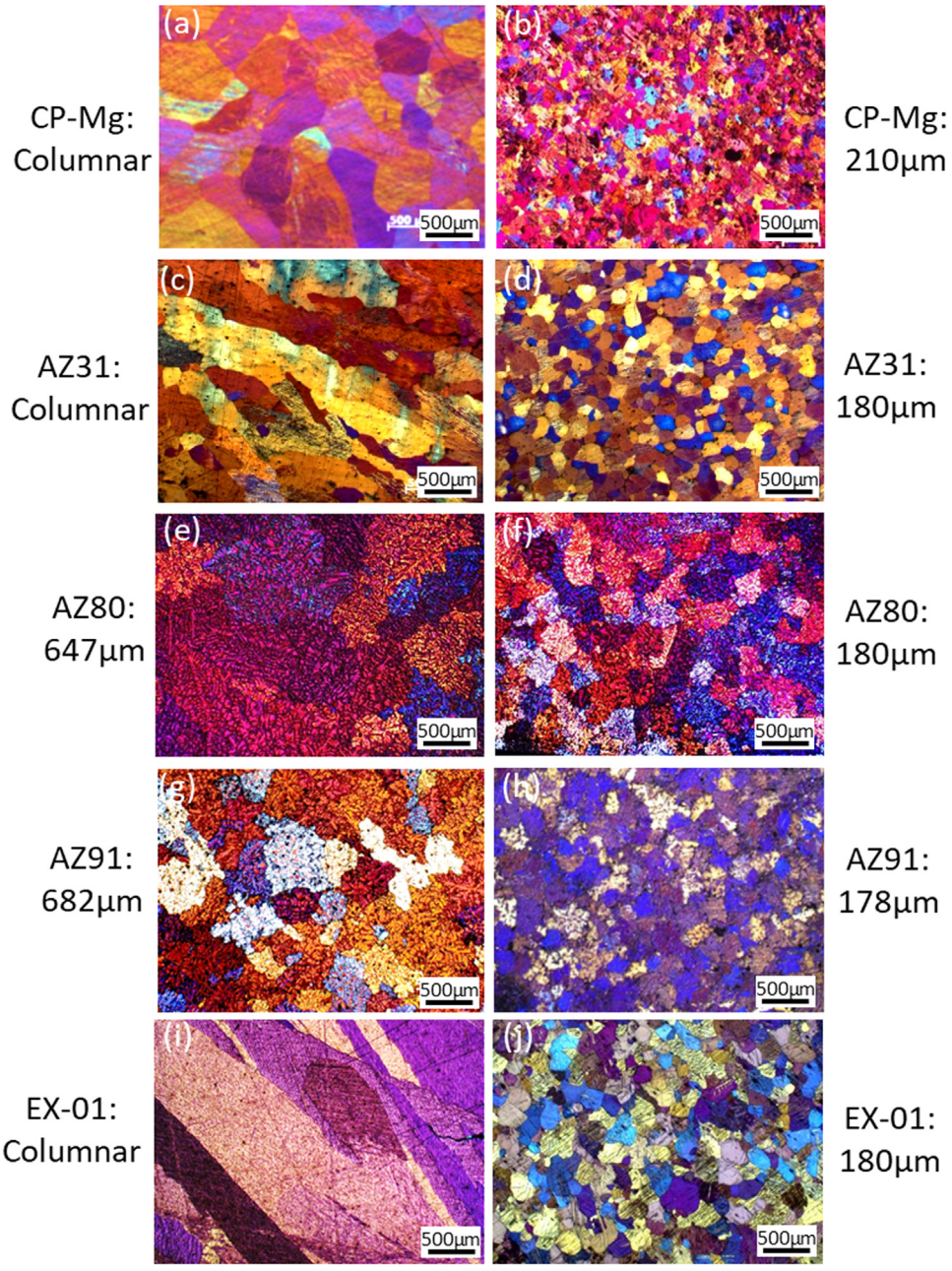

Fig. 37. The microstructures of various Mg alloys produced by conventional DC casting and MC-DC casting, showing that melt conditioning (intensive melt shearing) produces grain refinement of Mg alloys independent of alloys' compositions. (a,c,e,j,i) Conventional DC casting and (b, d, f, h, j) MC-DC casting.

180 μm while the grain size of the same alloys without melt shearing can be as large as 1 mm, or even columnar grains.

- The grain refining effect of intensive melt shearing can be sustained by repeated remelting and recasting without further intensive melt shearing (Fig. 31). This is attributed to the fact that the dispersed nano-sized native MgO particles will remain dispersed during remelting and act as the nucleation sites for grain refinement during the subsequent casting. New oxide films and potential surface contamination formed during remelting and casting make no significant difference to a population of highly impotent MgO particles with a high enough density.
- Intensive melt shearing is a process easy to implement in industrial casting processes for grain refinement. As we have demonstrated previously, it is suitable for HPDC, sand casting, DC casting, TRC and other casting processes.
- Intensive melt shearing provides not only grain refinement but also other advantages over chemical inoculation, such as enabling direct in-house recycling, and enhanced mechanical performance (particularly ductility, fatigue strength and fracture toughness) due to dispersed inclusions and secondary phase particles.

Overall, it can be concluded that grain refining Mg-alloys can be achieved through dispersing native MgO particles by

intensive melt shearing without the need for any exogenous grain refiners.

6. Concluding remarks

Grain refinement can increase the strength, ductility, formability and corrosion resistance of metallic alloys, and is particularly desirable for Mg-alloys. The conventional wisdom for grain refinement is to enhance heterogeneous nucleation through chemical inoculation by the addition of grain refiners that contain potent nucleant particles. Most recently, we have demonstrated that more significant grain refinement of Mg-alloys can be achieved by impeding heterogeneous nucleation using native MgO which is relatively impotent for heterogeneous nucleation of Mg. In this paper, we have provided a review of the traditional approaches to grain refinement and a detailed overview of the recent advances in understanding heterogeneous nucleation and grain initiation, and their implications for effective grain refinement of Mg-alloys. The major conclusions are summarised as follows:

- The native MgO exists in Mg-alloy melts as oxide films, which consist of densely populated MgO particles formed by direct oxidation of liquid Mg. Mg oxide films can be effectively dispersed into more discrete MgO particles by intensive melt shearing. The native MgO particles have a morphology of either octahedral or cubic with the {1 1 1} or {0 0 1} surface termination, respectively (denoted as MgO{1 1 1} and MgO{0 0 1}). The MgO particles have a log-normal particle size distribution with a geometrical mean size of $d_0 = 68$ nm and a standard deviation of $\sigma = 0.4$ for MgO{1 1 1}, and $d_0 = 85$ nm and $\sigma = 0.51$ for MgO{0 0 1}. The estimated effective MgO particle number density is 10^{14} and 10^{17} m^{-3} for Mg-alloy melts without and with intensive melt shearing, respectively.
- Native MgO has a lattice misfit of 7.9% with Mg, an atomically rough surface due to the existence of surface vacancies and surface atomic displacement, and is therefore relatively impotent for heterogeneous nucleation of Mg although it has been confirmed experimentally that both the MgO{1 1 1} and MgO{0 0 1} do nucleate Mg. The estimated nucleation undercooling ΔT_n for MgO/Mg system is 1.2 K, which is much larger than that for the TiB_2(Al_3Ti 2DC)/Al system ($\Delta T_n = 0.01$ K [145]).
- Grain initiation occurs during solidification in three distinctive modes: progressive grain initiation (PGI), explosive grain initiation (EGI) and hybrid grain initiation (HGI, and HGI = EGI + PGI). Such grain initiation behaviour can be well described in a grain initiation map. Generally, EGI is promoted by low cooling rate, low solute concentration, low nucleation potency and high nucleant particle density.
- We have developed an intensive melt shearing process, which was initially embodied by a twin-screw machine and later by a rotor-stator device. We have demonstrated that intensive melt shearing can effectively disperse the usual oxide films into more discrete MgO particles, which not only eliminates the harmful effect of oxide films but also uses positively the dispersed MgO particles for grain refinement.
- We found that the grain refining effect of intensive melt shearing can be sustained after repeated remelting and recasting without the need for further melt shearing. This suggests that intensive melt shearing prior to ingot casting can make Mg-alloys ingots self-grain-refining.
- The application of intensive melt shearing has led to the development of a range of melt-conditioned solidification processing technologies, such as MC-DC casting, MC-TRC, and MC-HPDC processes. Significant grain refinement has been achieved in all these melt-conditioned processes, resulting in a fine and uniform microstructure with substantially reduced cast defects.
- The traditional approach to grain refinement is to enhance heterogeneous nucleation by the selection of more potent nucleant particles to promote PGI. The new concept of EGI provides a novel approach to grain refinement, i.e., impeding heterogeneous nucleation by more impotent particles to promote EGI. We have used native MgO in Mg-alloys as an example to demonstrate this new approach.
- There is little space to develop grain refiners for Mg-alloys that can be more effective than native MgO particles. We have theoretically demonstrated and experimentally confirmed that the addition of more potent particles than MgO will not lead to more effective grain refinement than native MgO and that it is almost practically impossible to make MgO more impotent for further grain refinement. Therefore, we do not need to develop grain refiners for Mg-alloys, and what we need is to make the best use of the native MgO particles for effective grain refinement, such as the dispersion of native MgO particles by intensive melt shearing.

Declaration of Competing Interest

The authors declare that they have no known competing financial interests or personal relationships that could have appeared to influence the work reported in this paper.

Acknowledgment

Financial support from the EPSRC (UK) under grant number EP/N007638/1 is gratefully acknowledged.

References

[1] B.L. Mordike, T. Ebert, Mater. Sci. Eng. A 302 (2001) 37–45.
[2] H.E. Friedrich, B.L. Mordike, Magnesium Technology: Metallurgy, Design Data, Applications, Springer-Verlag, Berlin Heidelberg, Germany, 2006.
[3] I. Polmear, D. StJohn, J. Nie, M. Qian, Light Alloys: Metallurgy of the Light Metals, 5th ed., Elsevier Ltd, 2017.
[4] U. Riaz, I. Shabib, W. Haider, J. Bio. Mater. Res. Part B Appl. Biomater. 107 (2019) 1970–1996.
[5] L.A. Dobrzański, G.E. Totten, M. Bamberger, Magnesium and Its Alloys: Technology and Applications, CRC Press, Boca Raton, FL, USA, 2020.

[6] N. Loukil, T. Tański, P. Jarka, in: Magnesium Alloys Structure and Properties, IntechOpen, London, UK, 2022, pp. 183–193.
[7] Z.Z. Jin, M. Zha, S.Q. Wang, S.C. Wang, C. Wang, H.L. Jia, H.Y. Wang, J. Magnes. Alloy. 10 (2022) 1191–1206.
[8] K. Gusieva, C.H.J. Davies, J.R. Scully, N. Birbilis, Int. Mater. Rev. 60 (2015) 169–194.
[9] L.N. Zhang, Z.T. Hou, X. Ye, Z.B. Xu, X.L. Bai, P. Shang, Front. Mater. Sci. 7 (2013) 227–236.
[10] T. Tokunaga, M. Ohno, K. Matsuura, J. Mater. Sci. Technol. 34 (2018) 1119–1126.
[11] Z.Z. Yin, W.C. Qi, R.C. Zeng, X.B. Chen, C.D. Gu, S.K. Guan, Y.F. Zheng, J. Magnes. Alloy. 8 (2020) 42–65.
[12] K. Kubota, M. Mabuchi, K. Higashi, J. Mater. Sci. 34 (1999) 2255–2262.
[13] K.D. Ralston, N. Birbilis, Corrosion 66 (2010) 075005–075005-13.
[14] L. Wang, E. Mostaed, X. Cao, G. Huang, A. Fabrizi, F. Bonollo, C. Chi, M. Vedani, Mater. Des. 89 (2016) 1–8.
[15] Z. Zhang, J.H. Zhang, J. Wang, Z.H. Li, J.S. Xie, S.J. Liu, K. Guan, R.Z. Wu, Int. J. Miner. Metall. Mater. 28 (2021) 30–45.
[16] G. Nussbaum, P. Sainfort, G. Regazzoni, H. Gjestland, Scr. Metall. 23 (1989) 1079–1084.
[17] , in: Aluminium Handbok, 4nd ed., Japan Institute of Light Metals, Tokyo, 1990, p. 33.
[18] T. Mukai, K. Ishikawa, K. Higashi, Mater. Sci. Eng. A 204 (1995) 12–18.
[19] J. Koike, T. Kobayashi, T. Mukai, H. Watanabe, M. Suzuki, K. Maruyama, K. Higashi, Acta Mater. 51 (2003) 2055–2065.
[20] Y. Huang, Y. Wang, X. Meng, L. Wan, J. Cao, L. Zhou, J. Feng, J. Mater. Process. Technol. 249 (2017) 331–338.
[21] S.W. Xu, K. Oh-Ishi, H. Sunohara, S. Kamado, Mater. Sci. Eng. A 558 (2012) 356–365.
[22] M. Pekguleryuz, M. Celikin, Int. Mater. Rev. 55 (2010) 197–217.
[23] Y. Uematsu, K. Tokaji, M. Kamakura, K. Uchida, H. Shibata, N. Bekku, Mater. Sci. Eng. A 434 (2006) 131–140.
[24] Y. Estrin, A. Vinogradov, Int. J. Fatigue 32 (2010) 898–907.
[25] A. Yamashita, Z. Horita, T.G. Langdon, Mater. Sci. Eng. A 300 (2001) 142–147.
[26] Y. Estrina, A. Vinogradov, Acta Mater. 61 (2013) 782–817.
[27] A. Vinogradov, V.N. Serebryany, S.V. Dobatkin, Adv. Eng. Mater. 20 (2018) 1700785.
[28] K.K. Alaneme, E.A. Okotete, J. Magnes. Alloy. 5 (2017) 460–475.
[29] P. Mansoor, S.M. Dasharath, Mater. Today Proc. 20 (2020) 145–154.
[30] W. Wang, P. Han, P. Peng, T. Zhang, Q. Liu, S.N. Yuan, L.Y. Huang, H.L. Yu, K. Qiao, K.S. Wang, Acta Metall. Sin. 33 (2020) 43–57 (Eng. Lett.).
[31] H.J. Sharahi, M. Pouranvari, M. Movahedi, Mater. Sci. Eng. A 781 (2020) 139249.
[32] V. Patel, W. Li, A. Vairis, V. Badheka, Crit. Rev. Solid State Mater. Sci. 44 (2019) 378–426.
[33] R.Z. Valieva, T.G. Langdon, Prog. Mater. Sci. 51 (2006) 881–981.
[34] M. Avvari, S. Narendranath, H.S. Nayaka, Int. J. Mater. Prod. Technol. 51 (2015) 139–164.
[35] L.B. Tong, J.H. Chu, Z.H. Jiang, S. Kamado, M.Y. Zheng, J. Alloy. Compd. 785 (2019) 410–421.
[36] A.P. Zhilyaev, T.G. Langdon, Prog. Mater. Sci. 53 (2008) 893.
[37] R.B. Figueiredo, T.G. Langdon, Adv. Eng. Mater. 21 (2019) 1801039.
[38] D.G. Eskin, I. Tzanakis, F. Wang, G.S.B. Lebon, T. Subroto, K. Pericleous, J. Mi, Ultrason. Sonochem. 52 (2019) 455–467.
[39] S. Guo, Q. Le, Z. Zhao, Z. Wang, J. Cui, Mater. Sci. Eng. A 404 (2005) 323–329.
[40] S.F. Liu, L.Y. Liu, L.G. Kang, J. Alloy. Compd. 450 (2008) 546–550.
[41] L. Liu, X. Chen, F. Pan, J. Magnes. Alloy. 9 (2021) 1906–1921.
[42] Z. Fan, M. Xia, H. Zhang, G. Liu, J.B. Patel, Z. Bian, I. Bayandorian, Y. Wang, H.T. Li, G.M. Scamans, Int. J. Cast Met. Res. 22 (2009) 103–107.
[43] Z. Fan, Y. Wang, M. Xia, S. Arumuganathar, Acta Mater. 57 (2009) 4891–4901.
[44] H.T. Li, Y. Wang, Z. Fan, Acta Mater. 60 (2012) 1528–1537.
[45] J.B. Patel, X. Yang, C.L. Mendis, Z. Fan, JOM 69 (2017) 1071–1076.
[46] H.M. Fu, D. Qiu, M.X. Zhang, H. Wang, P.M. Kelly, J.A. Taylor, J. Alloy. Compd. 456 (2008) 390–394.
[47] D. Qiu, M.X. Zhang, J.A. Taylor, P.M. Kelly, Acta Mater. 57 (2009) 3052–3059.
[48] Y. Ali, D. Qiu, B. Jiang, F. Pan, M.X. Zhang, J. Alloy. Compd. 619 (2015) 639–651.
[49] D.H. StJohn, M. Qian, M. Easton, P. Cao, Z. Hildebrand, Metall. Mater. Trans. A 36 (2005) 1669–1679.
[50] D.H. StJohn, M.A. Easton, M. Qian, J.A. Taylor, Metall. Mater. Trans. A 44 (2013) 2935–2949.
[51] Z. Liu, Metall. Mater. Trans. A 48 (2017) 4755–4776.
[52] E. Karakulak, J. Magnes. Alloy. 7 (2019) 355–369.
[53] E.F. Emley, in: Principles of Magnesium Technology, Pergamon Press, Oxford, UK, 1966, pp. 126–156.
[54] D.H. StJohn, P. Cao, M. Qian, M.A. Easton, A Brief History of the Development of Grain Refinement Technology for Cast Magnesium Alloys, Magnes. Technol. (2013) 1–8, doi:10.1007/978-3-319-48150-0_1.
[55] The Future Liquid Metal Engineering Hub: Report (2015-2021). https://www.lime.ac.uk/blog/2021-annual-report-published. 2021 (accessed 23 September 2022).
[56] H. Men, Z. Fan, Metall. Mater. Trans. A 49 (2018) 2766–2777.
[57] B. Jiang, H. Men, Z. Fan, Comput. Mater. Sci. 153 (2018) 73–81.
[58] C.M. Fang, H. Men, Z. Fan, Metall. Mater. Trans. A 49 (2018) 6231–6242.
[59] C.M. Fang, Z. Fan, Metall. Mater. Trans. A 51 (2020) 788–797.
[60] C.M. Fang, Z. Fan, Comput. Mater. Sci. 171 (2020) 109258.
[61] C. Fang, S. Yasmin, Z. Fan, J. Phys. Commun. 5 (2021) 015007.
[62] H. Men, C.M. Fang, Z. Fan, Prenucleation at the Liquid/Substrate Interface: An Overview, Metals 12 (2022) 1704.
[63] Z. Fan, Metall. Mater. Trans. A 44 (2013) 1409–1418.
[64] Z. Fan, H. Men, Mater. Res. Express 7 (2020) 126501.
[65] Z. Fan, H. Men, Y. Wang, Z.P. Que, Metals 11 (2021) 478.
[66] Z. Fan, H. Men, Metals 12 (2022) 1547.
[67] Z. Fan, H. Men, Metals 12 (2022) 1454.
[68] Z. Fan, in: Proceedings of the 11th International Conference Magnesium Alloys and Their Applications, Beaumont Estate, Old Windsor, UK, 2018, pp. 7–17.
[69] Z. Fan, F. Gao, B. Jiang, Z.P. Que, Impeding nucleation for more significant grain refinement, Sci. Rep. 10 (2020) 9448.
[70] Z. Fan, F. Gao, Grain Initiation and Grain Refinement: An Overview, Metals 12 (2022) 1728.
[71] Z. Fan, F. Gao, Y. Wang, H. Men, L. Zhou, Prog. Mater. Sci. 123 (2022) 100809.
[72] O. Madelung, U. Rössler, M. Schulz, Magnesium Oxide (MgO) Crystal Structure, Lattice Parameters, Thermal Expansion, Springer Materials, 1999 The Landolt-Brnstein-Group III Condensed Matter 41B https://materials.springer.com/lb/docs/sm_lbs_978-3-540-31359-5_206 .
[73] P.W. Tasker, Philos. Mag. A 39 (1979) 119–136.
[74] C.M. Fang, M.A. van Huis, D. Vanmaekelbergh, H.W. Zandbergen, ACS Nano 4 (2010) 211–218.
[75] J. Campbell, Castings, 2nd ed., Butterworth-Heinemann, Oxford, UK, 2003.
[76] S.H. Wang, Y. Wang, Q. Ramasse, Z. Fan, Metall. Mater. Trans. A 51 (2020) 2957–2974.
[77] G. Pettersen, E. Øvrelid, G. Tranell, J. Fenstad, H. Gjestland, Mater. Sci. Eng. A 332 (2002) 285–294.
[78] G.S. Peng, Y. Wang, Z. Fan, Metall. Mater. Trans. A 49 (2018) 2182–2192.
[79] Y. Wang, Z. Fan, X. Zhou, G.E. Thompson, Philos. Mag. Lett. 91 (2011) 516–529.
[80] Z. Fan, Y. Wang, Y. Zhang, T. Qin, X.R. Zhou, G.E. Thompson, T. Pennycook, T. Hashimoto, Acta Mater. 84 (2015) 292–304.
[81] Y. Wang, G.S. Peng, Z. Fan, K. Solanki, D. Orlov, A. Singh, N. Neelameggham, in: Mg Technology, 2017, TMS, Springer, 2017, pp. 99–106.

[82] H. Men, B. Jiang, Acta Mater. 58 (2010) 6526–6534.
[83] T.E. Quested, A.L. Greer, Acta Mater. 52 (2004) 3859–3868.
[84] T.A. Engh, Principles of Metal Refining, Oxford University Press, UK, 1992.
[85] S.L. Sin, A. Elsayed, C. Ravindran, Int. Mater. Rev. 58 (2013) 419–436.
[86] P. Bakke, D.O. Karlsen, Inclusion assessment in magnesium and magnesium base alloys, SAE Transactions 106 (1997) 314–326 http://www.jstor.org/stable/44657572.
[87] , Standard Test Procedure for Al Alloy Grain Refiners (TP-1), The Al Association, Washington, DC, 1990.
[88] Z. Fan, F. Gao, L. Zhou, S.Z. Lu, Acta Mater. 152 (2018) 248–257.
[89] L. Zhou, The role of various solutes on grain refinement of aluminium alloys with Al-Ti-B inoculations, PhD Thesis, Brunel University London, UK, 2015.
[90] B. Jiang, PhD Thesis, Brunel University London, UK, 2013.
[91] A.V. Nagasekhar, M.A. Easton, C.H. Cáceres, Adv. Eng. Mater. 11 (2009) 912–919.
[92] Z. Fan, M. Xia, Z. Bian, I. Bayandorian, L. Cao, H. Li, G.M. Scamans, Mater. Sci. Forum 649 (2010) 315–323.
[93] J. Lazaro-Nebreda, J.B. Patel, Z. Fan, J. Mater. Process. Technol. 294 (2021) 117146.
[94] Z. Fan, Y.B. Zuo, B. Jiang, Mater. Sci. Forum 690 (2011) 141–144.
[95] Z. Fan, Mater. Sci. Eng. A 413 (2005) 72–78.
[96] Z. Fan, B. Jiang, Y.B. Zuo, Apparatus and method for liquid metals treatment, US Patent US9498820B2, 2016.
[97] F. Bonollo, N. Gramegna, G. Timelli, JOM 67 (2015) 901–908.
[98] S. Tzamtzis, H. Zhang, G. Liu, Y. Wang, N.H. Babu, Z. Fan, Melt conditioned high pressure die casting (Mc-HPDC) of Mg-Alloys, Proc. Conf. on Magnesium technology, TMS (2009) 91–96.
[99] S. Tzamtzis, H. Zhang, M. Xia, N.H. Babu, Z. Fan, Mater. Sci. Eng. A 528 (2011) 2664–2669.
[100] S. Tzamtzis, H. Zhang, N.H. Babu, Z. Fan, Mater. Sci. Eng. A 527 (2010) 2929–2934.
[101] M. Xia, S. Mitra, B. Dhindaw, G. Liu, Z. Fan, Metall. Mater. Trans. B 41 (2010) 209–213.
[102] S.M. Liang, H.W. Zhang, M.X. Xia, R.S. Chen, E.H. Han, Z. Fan, Trans. Nonferrous Met. Soc. China 20 (2010) 1205–1211.
[103] S. Ji, W. Yang, B. Jiang, J.B. Patel, Z. Fan, Mater. Sci. Eng. A 566 (2013) 119–125.
[104] Y. Zhang, J.B. Patel, Y. Wang, Z. Fan, Mater. Charact. 144 (2018) 498–504.
[105] Y. Zhang, J.B. Patel, J. Lazaro-Nebreda, Z. Fan, JOM 70 (2018) 2726–2730.
[106] Y. Zhang, S.H. Wang, E. Lordan, Y. Wang, Z. Fan, J. Alloy. Compd. 785 (2019) 1015–1022.
[107] E. Lordan, J. Lazaro-Nebreda, Y. Zhang, Z. Fan, JOM 71 (2019) 824–830.
[108] J. Grandfield, D.G. Eskin, I. Bainbridge, Direct-Chill Casting of Light Alloys: Science and Technology, John Wiley & Sons, Inc., Hoboken, New Jersey, US, 2013.
[109] R. Haghayeghi, Y. Liu, Z. Fan, Solid State Phenom. 141 (2008) 403–408.
[110] Y.B. Zuo, B. Jiang, Z. Fan, Mater. Sci. Forum 690 (2011) 137–140.
[111] Y.B. Zuo, B. Jiang, Y. Zhang, Z. Fan, IOP Conf. Ser. Mater. Sci. Eng. 27 (2012) 012043.
[112] Y.B. Zuo, B. Jiang, Y. Zhang, Z. Fan, Melt Conditioned DC (MC-DC) Casting of Magnesium Alloys, Magnes. Technol. (2012) 155–160, doi:10.1007/978-3-319-48203-3_29.
[113] M.X. Xia, A.K. Prasada Rao, Z. Fan, Mater. Sci. Forum 765 (2013) 291–295.
[114] H.T. Li, P. Zhao, R. Yang, J.B. Patel, X.F. Chen, Z. Fan, Metall. Mater. Trans. B 48 (2017) 2481–2492.
[115] K. Al-Helal, J.B. Patel, G.M. Scamans, Z. Fan, Materials 13 (2020) 5740.
[116] K. Al-Helal, J.B. Patel, G.M. Scamans, Z. Fan, Materials 13 (2020) 2711.
[117] N.S. Barekar, I. Skalicky, C. Barbatti, Z. Fan, M. Jarrett, J. Alloy. Compd. 862 (2021) 158008.
[118] K.M. Sree Manu, N.S. Barekar, J. Lazaro-Nebreda, J.B. Patel, Z. Fan, J. Mater. Process. Technol. 295 (2021) 117170.
[119] G.S.B. Lebon, H.T. Li, J.B. Patel, H. Assadi, Z. Fan, Appl. Math. Model. 77 (2020) 1310–1330.
[120] W.J. Boettinger, S.R. Coriell, A.L. Greer, A. Karma, W. Kurz, M. Rappaz, R. Trivedi, Acta Mater. 48 (2000) 43–70.
[121] R. Cook, P.G. Grocock, P.M. Thomas, D.V. Edmonds, J.D. Hunt, J. Mater. Process. Technol. 55 (1995) 76–84.
[122] S.S. Park, W.J. Park, C.H. Kim, B.S. You, N.J. Kim, JOM 61 (2009) 14–18.
[123] A. Javaid, F. Czerwinski, J. Magnes. Alloy. 9 (2021) 362–391.
[124] N.S. Barekar, S. Das, Z. Fan, Mater. Sci. Forum 794 (2014) 1115–1120.
[125] Z. Bian, I. Bayandorian, H.W. Zhang, Z. Fan, Solid State Phenom. 141 (2008) 195–200.
[126] Z. Bian, I. Bayandorian, H.W. Zhang, G. Scamans, Z. Fan, Mater. Sci. Technol. 25 (2009) 599–606.
[127] I. Bayandorian, Z. Bian, M. Xia, H. Zhang, G.M. Scamans, Z. Fan, Magnes. Technol. TMS (2009) 363–368 (The Minerals, Metals & Materials Society).
[128] S. Das, S. Ji, O. El Fakir, L.L. Wang, J.P. Dear, J.G. Lin, I. Stone, G. Scamans, Z. Fan, Mater. Sci. Forum 765 (2013) 170–174.
[129] S. Das, N. Barekar, O. El Fakir, X. Yang, J.P. Dear, Z. Fan, Mater. Lett. 144 (2015) 54–57.
[130] S. Das, N.S. Barekar, O. El Fakir, L. Wang, A.K. Prasada Rao, J.B. Patel, H.R. Kotadia, A. Bhagurkar, J.P. Dear, Z. Fan, Mater. Sci. Eng. A 620 (2015) 223–232.
[131] N.S. Barekar, S. Das, X. Yang, Y. Huang, O. El Fakir, A.G. Bhagurkar, L. Zhou, Z. Fan, Mater. Sci. Eng. A 650 (2016) 365–373.
[132] K. Al-Helal, J.B. Patel, Z. Fan, JOM 71 (2019) 1714–1721.
[133] K. Al-Helal, I. Chang, J.B. Patel, Z. Fan, JOM 71 (2019) 2018–2024.
[134] A. Nag, P. Kota, N. Agrawal, A. Bhandari, N. Singh, P. Ray, P. Patil, S. Das, Mater. Lett. 240 (2019) 295–298.
[135] K. Al-Helal, J.B. Patel, Z. Fan, JOM 72 (2020) 3753–3759.
[136] J.B. Patel, P. Lloyd, G. Peng, Z. Fan, Development of the New High Shear Technology for Continuous Processing of Mg-Alloys for Ingot Casting, Magnes. Technol. (2016) 29–33, doi:10.1007/978-3-319-48114-2_8.
[137] J.B. Patel, Y. Zhang, Z. Fan, in: LiME Hub: report 2015-2021, 2021, pp. 86–87. (https://www.lime.ac.uk/blog/2021-annual-report-published).
[138] G. Liu, Y. Wang, Z. Fan, Mater. Sci. Eng. A 472 (2008) 251–257.
[139] A.L. Greer, J. Chem. Phys. 145 (2016) 211704.
[140] M.A. Easton, M. Qian, A. Prasad, D.H. StJohn, Curr. Opin. Solid State Mater. Sci. 20 (2016) 13–24.
[141] Y. Wang, C.M. Fang, L. Zhou, T. Hashimoto, X. Zhou, Q.M. Ramasse, Z. Fan, Acta Mater. 164 (2019) 428–439.
[142] S.H. Wang, Characterisation of Native MgO and Its Roles in Solidification of Mg Alloys, PhD Thesis, Brunel University London, UK, 2020.
[143] Y. Wang, S.H. Wang, Z.P. Que, C.M. Fang, T. Hashimoto, X.R. Zhou, Q.M. Ramasse, Z. Fan, Manipulating Nucleation Potency of Substrates by Interfacial Segregation: An Overview, Metals 12 (2022) 1636.
[144] S.H. Wang, F. Wang, Y. Wang, Q.M. Ramasse, Z. Fan, IOP Conf. Ser. Mater. Sci. Eng. 529 (2019) 012048.
[145] A.L. Greer, A.M. Bunn, A. Tronche, P.V. Evans, D.J. Bristow, Acta Mater. 48 (2000) 2823–2835.